University of Maribor
Faculty of Energy Technology

Journal of ENERGY TECHNOLOGY

Volume 16 / Issue 3
NOVEMBER 2023
www.fe.um.si/en/jet.html

Journal of ENERGY TECHNOLOGY

VOLUME 16 / Issue 3

Revija Journal of Energy Technology (JET) je indeksirana v bazah INSPEC© in Proquest's Technology Research Database.

The Journal of Energy Technology (JET) is indexed and abstracted in database INSPEC© and Proquest's Technology Research Database.

JOURNAL OF ENERGY TECHNOLOGY

Tehnični urednik / TECHNICAL EDITOR

Sonja KRANJC

Tehnična podpora / TECHNICAL SUPPORT

Tamara BREČKO BOGOVČIČ

Izhajanje revije / PUBLISHING

Revija izhaja štirikrat letno v nakladi 100 izvodov. Članki so dostopni na spletni strani revije - www.fe.um.si/si/jet.html / The journal is published four times a year. Articles are available at the journal's home page - www.fe.um.si/en/jet.html.

Cena posameznega izvoda revije (brez DDV) / Price per issue (VAT not included in price): 50,00 EUR.

Informacije o naročninah / Subscription information:
http://www.fe.um.si/en/jet/subscriptions.html

Lektoriranje / LANGUAGE EDITING

TAIA INT d.o.o.

Oblikovanje in tisk / DESIGN AND PRINT

Tiskarna Saje d.o.o.

Naslovna fotografija / COVER PHOTOGRAPH

Jurij AVSEC

Oblikovanje znaka revije / JOURNAL AND LOGO DESIGN

Andrej PREDIN

Ustanovni urednik / FOUNDING EDITOR

Andrej PREDIN

Izdajanje revije JET finančno podpira Javna agencija za raziskovalno dejavnost Republike Slovenije iz sredstev državnega proračuna iz naslova razpisa za sofinanciranje domačih znanstvenih periodičnih publikacij / The Journal of Energy Technology is co-financed by the Slovenian Research Agency.

Spoštovani bralci revije Journal of energy technology (JET)

Leta 2022 je bila skupna poraba energije v Sloveniji približno 6570 ktoe (kiloton olja ekvivalentno), kar je približno 3,1 toe na prebivalca. Dobra četrtina vse porabljene energije v Sloveniji predstavlja poraba električne energije.

Danes je elektroenergetika eden od najpomembnejših stebrov energetike, saj električna energija poganja dobršen del naprav. Njena uporaba je vidna na vseh korakih od pogona hladilnikov, brivnikov, pralnih strojev, računalnikov, indukcijskih in elektrouporovnih pečeh v industriji pa vse do električnih kosilnic in električnih avtomobilov ter vlakov.

Zgodovina razvoja elektroenergetike se začenja okoli leta 600 pred našim štetjem. Zapisi Talesa iz Mileta iz stare Grčije kažejo, da so takrat nevede odkrili pojav statične elektrike. Prvič je bila beseda elektrika omenjena okoli leta 1600, ko je angleški znanstvenik Gilberto iz grškega izraza skoval novo latinsko besedo electricus, ki so jo nato prevzeli vsi drugi jeziki. Razvoj elektroenergetike se je intenzivno nadaljeval v naslednjih stoletjih. V 19. stoletju so se pojavile prve hidroelektrarne in vodne elektrarne (ZDA). Prva javna razsvetljava je bila v Sloveniji vpeljana konec 19. stoletja, kmalu po izumu žarnice na ogleno nitko. Dvajseto stoletje pa je zaznamoval začetek masovne uporabe električnih naprav. Prva električna luč je na Slovenskem zasvetila v Mariboru leta 1883. Pri razvoju elektroenergetike so sodelovali nekateri vidni predstavniki Slovenije, Hrvaške in Srbije, med drugim Nikola Tesla, Mihajlo Pupin, Milan Vidmar.

Razvoj elektroenergetike tudi danes poteka z veliko hitrostjo. Zelo pomembno je, da raziskovalci aktivno sodelujejo pri razvoju elektroenergetike. V tokratni izdaji revije JET je kar nekaj zanimivih člankov s področja elektroenergetike. Vsem bralcem želim zanimivo branje.

Jurij AVSEC
odgovorni urednik revije JET

Dear Readers of the Journal of Energy Technology (JET)

In 2022, the total energy consumption in Slovenia was approximately 6,570 ktoe (kilotons of oil equivalent), which amounts to approximately 3.1 toe per inhabitant. A good quarter of all the energy used in Slovenia is electricity consumption.

Today, it represents electrical energy, one of the most important pillars of energy. Electricity powers a good number of devices today. Today, the use of electricity can be seen at every step, from powering refrigerators, shavers, washing machines, computers, induction and electric resistance furnaces in industries, all the way to electric lawn mowers and electric cars and trains.

The very history of the development of electric power begins around 600 BC with the writings of Thales of Miletus from ancient Greece, who unknowingly discovered the phenomenon of static electricity at that time. The word electricity was first mentioned around 1600 with the help of the English scientist Gilbert, who coined the new Latin word electricus from the Greek term, which was adopted by all other languages. The development of electric power continued intensively in the following centuries. In the 19th century the first hydroelectric power plants and water power plants appeared (USA). The first public lighting was introduced in Slovenia at the end of the 19th century, shortly after the invention of the coal filament light bulb. The twentieth century marks the beginning of the mass use of electrical devices. The first electric light in Slovenia was lit in Maribor in 1883. Some prominent representatives of the areas of present-day Slovenia, Croatia and Serbia took part in the development of electric power.. Nikola Tesla, Mihajlo Pupin, Milan Vidmar...

The development of electric engineering continues today at a high speed. It is very important that, even today, researchers participate actively in the development of electric power engineering. The presented edition of the JET magazine presents quite a few interesting articles in the field of Power Engineering. I wish all readers an interesting reading of JET magazine.

Jurij AVSEC
Editor-in-chief of JET

Table of Contents
Kazalo

Journal of Energy Technology

JET Volume 16 (2023) p.p. 11-21
Issue 3, 2023
Type of article: 1.01
http://www.fe.um.si/si/jet.htm

THE INFLUENCE OF UNBALANCED CURRENT IN BUS BARS ON MAGNETIC FIELD DISTRIBUTION

VPLIV NEURAVNOTEŽENEGA TOKA V ELEKTRIČNIH ZBIRALKAH NA PORAZDELITEV MAGNETNEGA POLJA

Miodrag Milutinov [1]✉, Karolina Kasaš Lažetić [1], Teodora Spasić [1], Miroslav Prša [2]

Keywords: current unbalance, magnetic field, three phase, bus bar

Abstract

The analysis of magnetic field and current density distribution in the case of a three phase bus bar system with a current of 500 A is presented in this paper. The impact is investigated of the position of the neutral conductor on the magnetic field and current density distribution. The main goal of the calculations was to find the position of the neutral conductor which produces the lowest magnetic field and current density in the case of current unbalance. The numerical calculations were performed in the COMSOL Multiphysics program package on a simplified 2D model. The calculation results are presented graphically, as the diagrams of the magnetic flux and current density magnitude distribution in the three-phase bus bar system plane, are perpendicular to the system's axis. The obtained results show that, in both cases, (current balance and current unbalance), the position of the neutral conductor influences the magnetic flux density distribution.

Povzetek

V prispevku je predstavljena analiza porazdelitve magnetnega polja in gostote toka v primeru trifaznega zbiralnega sistema s tokom 500 A. Raziskuje se vpliv položaja nevtralnega vodnika na magnetno polje in porazdelitev gostote toka. Glavni cilj izračunov je bil najti položaj nevtralnega vodnika, ki proizvaja najmanjše magnetno polje in gostoto toka v primeru tokovne

✉ Corresponding author: Prof. Miodrag Milutinov, University of Novi Sad, Faculty of Technical Sciences, Trg Dositeja Obradovića 6, 21000 Novi Sad, Serbia, Tel.: +381 63 352 601, E-mail address: miodragm@uns.ac.rs

1 University of Novi Sad, Faculty of Technical Sciences, Trg Dositeja Obradovića 6, 21000 Novi Sad, Serbia

2 Retired from the University of Novi Sad, Faculty of Technical Sciences

neuravnoteženosti. Numerični izračuni so bili izvedeni v programskem paketu COMSOL Multiphysics na poenostavljenem 2D-modelu. Rezultati izračuna so predstavljeni grafično kot diagrami porazdelitve magnitude magnetnega pretoka in gostote toka v ravnini trifaznega sistema zbiralk, pravokotni na os sistema. Dobljeni rezultati kažejo, da v obeh primerih (tokovno ravnotežje in tokovno neuravnoteženost) položaj nevtralnega vodnika vpliva na porazdelitev gostote magnetnega pretoka.

1 INTRODUCTION

Parts of a power delivery system, such as distribution lines, generate a magnetic field at a frequency of 50/60 Hz, which belongs to the extremely low frequency range (ELF) from 3 Hz to 3 kHz. Depending on the intensity, this magnetic field could have influence on various biological systems, both by short and continuous exposure [1][2]. The level of the adverse effect depends on the magnetic field`s magnitude and frequency. Two common magnetic field quantities are the magnetic field strength and the magnetic flux density, denoted by H and B, respectively. Although the influence of magnetic fields on the human body and tissue is complex, these two quantities are used to estimate the potential adverse health effect. Based on extensive scientific literature, the International Commission on Non-Ionizing Radiation Protection (ICNIRP) proposed the so-called referenced level for the occupational and general public exposure to electromagnetic fields (EMF) [3], which became the basis for national legislation worldwide, and it was adopted without any changes. The reference levels are used for easy and quick estimation of adverse health effects by comparing their value with the measured/calculated values. The reference levels of the magnetic field and the magnetic flux density for general public exposure at the frequency of 50/60 Hz are 160 A/m and 200 μT, respectively, as prescribed by ICNIRP. These reference levels for public exposure to EMF became the basis for national legislation worldwide. Many countries have adopted these levels without any changes. Serbia's national legislation [4], prescribes five times lower values; 32 A/m of magnetic field intensity and 40 μT of magnetic flux density vector magnitude, which are considerably lower, and ensure additional safety for the general public. Both physical quantities must be measured or calculated in free space (in air) around the current carrying conductors. In a vacuum the magnetic field strength and the magnetic flux density (MFD) are related trough the vacuum permeability expressed by the following equation

$$B = \mu_0 H \tag{1.1}$$

where the vacuum permeability is a constant, taking the value of $\mu_0 = 4\pi \cdot 10^{-7}\,\mathrm{H/m}$. The same relation could be used in the air around the conductor allowing measurement or calculation of only one of the quantities.

The magnitude of the MFD generated by distribution lines depends on the currents and geometry of the system, as shown in [5]-[7]. In a three-phase system, the currents in the phase conductors are expressed by

$$\begin{aligned} i_1 &= I_1\sqrt{2}\cos\left(\omega t + \psi_1\right), \\ i_2 &= I_2\sqrt{2}\cos\left(\omega t + \psi_2\right), \\ i_3 &= I_3\sqrt{2}\cos\left(\omega t + \psi_3\right). \end{aligned} \tag{1.2}$$

By aligning the conductors with the z direction of the Cartesian coordinate system an MFD has only x and y components, as depicted in Fig. 1. Pair $k-\text{th}$ present the coordinate of the centre line of the $k-\text{th}$ conductor, while pair (x,y) present the coordinate of the point in the plane.

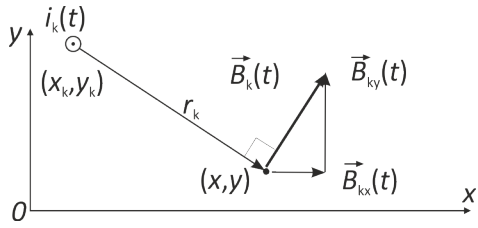

Figure 1: *MFD vector in the plane perpendicular to the conductors*

The net x and y component of MFD is equal to the following sums:

$$B_x(x,y,t) = -\frac{\mu_0}{2\pi}\sum_{k=1}^{3}\frac{i_k(t)}{r_k^2}\left(y-y_k\right), \tag{1.3}$$

$$B_y(x,y,t) = \frac{\mu_0}{2\pi}\sum_{k=1}^{3}\frac{i_k(t)}{r_k^2}\left(x-x_k\right). \tag{1.4}$$

The intensity and orientation of the MFD at any point in the xy plane besides the positions of the conductors and amplitudes of the currents, depends on the phase arrangement. In a three-phase circuit, the system could be balanced or unbalanced. A three-phase circuit is balanced if the phase currents are of the same amplitudes and the phase of each current is shifted 120° from each other. If either or both conditions are not met, the circuit is unbalanced [8].

The usual assumption is that currents are balanced, where an unbalanced current could affect the magnetic field distribution additionally [9]-[12]. In a power transmission subsystem with only three phase conductors the three-phase circuit is nearly balanced, where several ways to quantify the current unbalance existed in the literature. Some of them are used in the author's previous works [13]-[15], where it was presented how the current unbalance affects the magnetic field distribution in the vicinity of the power lines. In these papers the authors showed that a magnetic field generated by an unbalanced circuit drops more slowly with distance than in the balanced case. Also, they tried to find the correlation between current unbalance and MFD deviation.

The power delivery subsystem has an additional, so-called neutral conductor, with instantaneous current i_0 equal to the sum of the three phase currents, expressed by

$$i_0(t) = i_1(t) + i_2(t) + i_3(t)\,. \tag{1.5}$$

The current in the neutral conductor is in the opposite direction, and generates an additional magnetic field, which reduces the net magnetic field. The influence of current unbalance in a 3+1 subsystem on the magnetic flux density magnitude and polarisation of the magnetic field is presented in the author's previous works [16]-[19]. In this paper, the influence is examined of the neutral conductor position that provides the lowest magnetic field outside the system. It is assumed that the currents are phase shifted by 120° from each other, and only amplitude unbalance is considered.

2 MODEL

A model of the energy bus bar system from the E-LINE-KX catalogue produced by EAE Corporate is analysed in this paper [20]. It was created with sheets of insulated copper conductors placed in a closed aluminium housing, as shown in Fig. 2. According to the manufacturer`s information, the rated current I_R of the analysed bus bar is 500 r.m.s. This rated current was used for the MFD calculation.

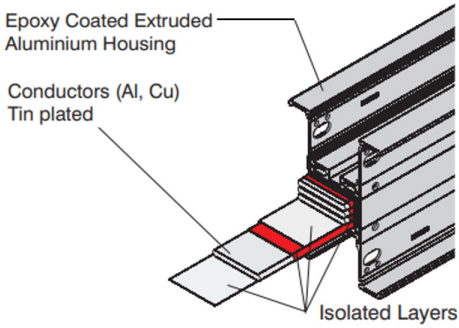

Figure 2: *Analysed bus taken from the catalogue [20]*

The cross-section of the model with dimensions expressed in (mm) is shown in Fig. 3. The cross-section of each copper conductor is $6 \times 25\,\text{mm}^2$ coated with 1 mm epoxy as isolation between the conductors. The conductors are labelled with numbers 1, 2, 3, and 0, where the numbers from 1 to 3 correspond to phase currents, and 0 presents the neutral conductor.

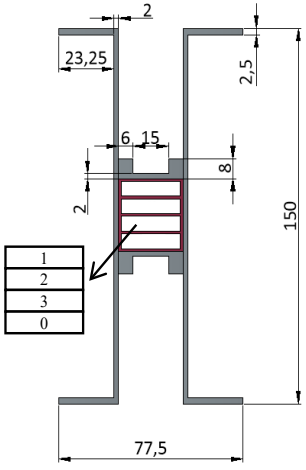

Figure 3: *The cross-section of the analysed bus bar*

Calculation of the current density distribution inside the conductors and the magnetic flux density in the air around the bus bar was done in the COMSOL Multiphysics software package, which

solves partial differential equations using the Finite Element Method. For these calculations a 2D model of the system was created, and the following equations were applied

$$\sigma\frac{\partial\vec{A}}{\partial t}+\nabla\times\left(\frac{1}{\mu}\nabla\times\vec{A}\right)=\vec{J}_e, \tag{2.1}$$

$$\vec{J}=-\sigma\frac{\partial\vec{A}}{\partial t} \tag{2.2}$$

where σ and $\vec{J}_e$ are the conductivity and the permeability of the material applied in the model, $\vec{J}_e$ is the applied external current density, $\vec{A}$ is the induced current density, and $\vec{A}$ is the magnetic vector potential. The magnetic flux density was calculated by the following equation

$$\nabla\times\vec{B}=\frac{1}{\mu}\left(\vec{J}+\vec{J}_e\right) \tag{2.3}$$

The influence of the position of the neutral conductor on the current density distribution and the magnetic flux density distribution was analysed in the balanced and the unbalanced cases.

In the balanced case, the rated current $=500\text{A}$ was applied to all three phase conductors. In the unbalanced case the current in one of the phase conductors was assumed to be up to 20% lower. For example, the notation 1-1-0.8 means that $I_1=I_R$, $I_2=I_R$ and $I_3=0.8I_R$. Additionally, the magnitude of the magnetic flux density vector was calculated along the *x*-axis outside the bus bar housing. Comparing the magnitudes of the magnetic flux density in both the balanced (denoted with B_0) and unbalanced cases (denoted with *B*), the relative deviation was calculated as

$$\delta B=\frac{B-B_0}{B_0}\cdot 100\% \tag{2.4}$$

3 RESULTS

Fig. 4 shows the MFD distribution inside the bus bar in the balanced case at 50 Hz for all possible positions of the neutral conductor. In the balanced case there was no external current applied to the neutral conductor. The induced current in the neutral conductor is negligible at a frequency of 50 Hz, therefore, the position of the neutral conductor impacts the magnetic field only by increasing the spatial distance between the phase conductors.

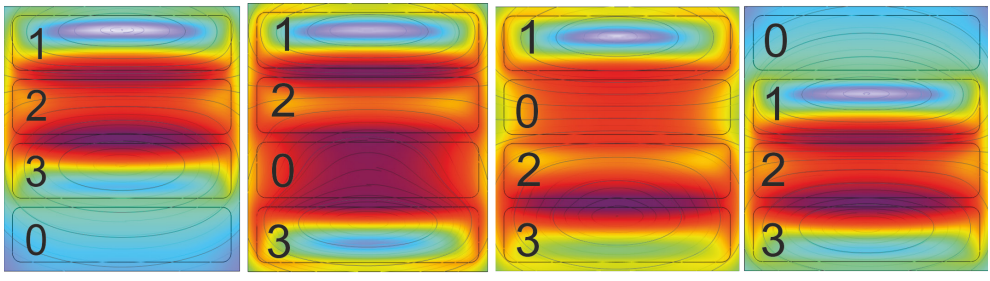

Figure 4: *MFD distribution inside the bus bar in the balanced case at 50 Hz*

The induced current in the neutral conductor increases by increasing the frequency of the external applied current. Repeating the calculations at a frequency of 450 Hz MFD distribution inside the bus bar are shown in Fig. 5. This frequency was chosen as the 9-th harmonic of the fundamental frequency. At this frequency skin effect and proximity effect affect the MFD distribution.

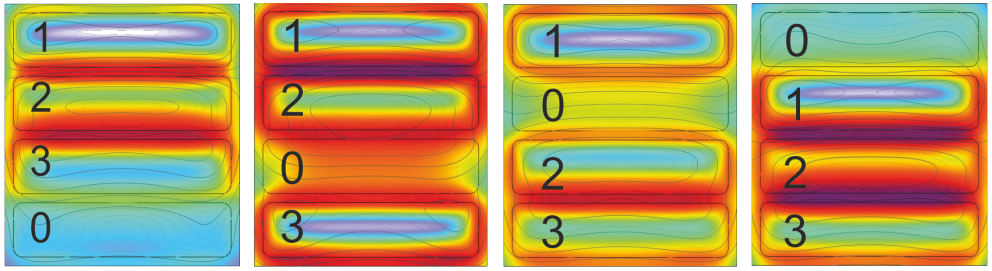

Figure 5: *MFD distribution inside the bus bar in the balanced case at 450 Hz*

Figs. 6 and 7 show the MFD distribution outside the bus bar at 50 Hz and 450 Hz in the balanced case, respectively. The position of the neutral conductor impacts the distribution of the MFD only near the bus bar. Increasing the distance from the bus bar this impact becomes negligible.

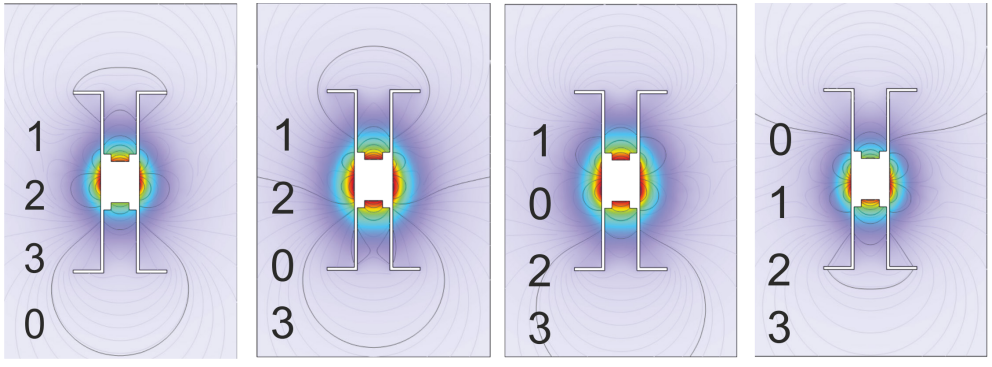

Figure 6: *MFD distribution outside the bus bar in the balanced case at 50 Hz*

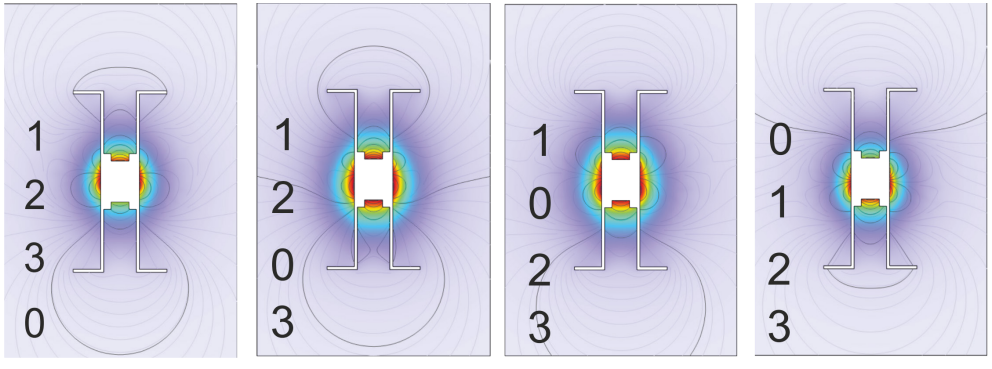

Figure 7: *MFD distribution outside the bus bar in the balanced case at 50 Hz*

In the case of an unbalanced current, the MFD had a different distribution, even further from the bus bar. Increasing the unbalance, the MFD becomes more dependent on the position of the neutral conductor. The MFD distribution in the unbalanced case, when the current in the third conductor was $I_3 = 0.8 I_R$, is shown in Fig. 8.

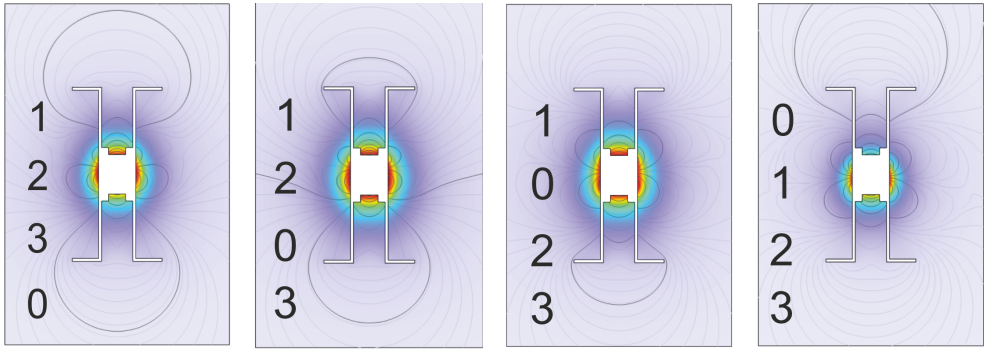

Figure 8: *MFD distribution outside the bus bar in the unbalanced case 1-1-0.8, at 50 Hz*

MFDs calculated only along the *x*-axis for all four positions of the neutral conductor in the balanced and unbalanced cases are shown in Fig. 9 and Fig. 10, respectively. The magnitude of the MFD was calculated outside of the bus bars, starting at x =20 mm from an origin located in the centre of the bus bar. It can be seen in more detail how the MFD magnitude depends on the position of the neutral conductor. In the balanced case (Fig. 9) the magnitude decreases faster if the neutral conductor is outside the deck, (see lines labelled 1230 and 0123). The reference levels of 200 uT and 40 uT were reached at about 65 mm and 140 mm outside of the bus bar, respectively. In the unbalanced case (Fig. 10) for the current combination 1-1-0.8, the lowest MFD occurred for the 0123 layout, when the neutral conductor was located furthest from the conductor with the lower current. Other combinations, for example, 1-0.8-1 or 0.9-1-1, give different positions of the neutral conductor that generated the lowest MFD.

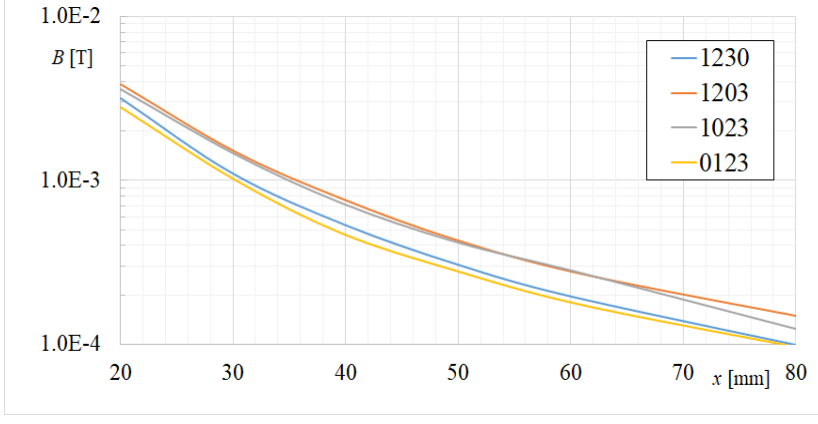

Figure 9: *MFD distribution outside the bus bar in the unbalanced case 1-1-0.8, at 50 Hz*

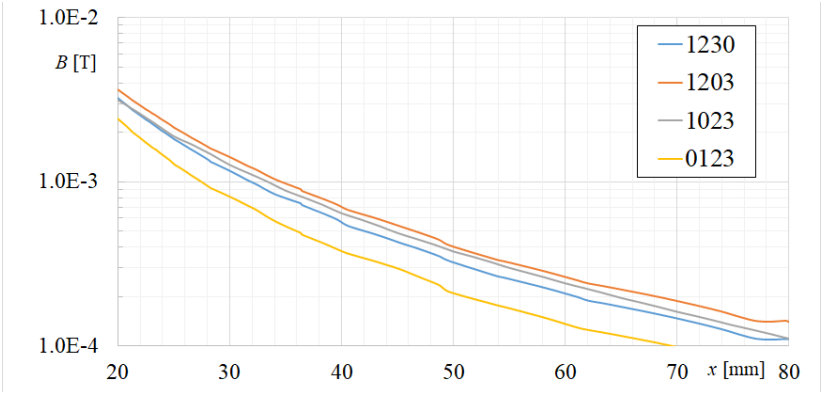

Figure 10: *MFD distribution outside the bus bar in the unbalanced case 1-1-0.8, at 50 Hz*

By analysing all the combinations of currents and positions of the neutral conductors and applying equation (2.4), the relative deviation of the magnitude of the MFD along the x-axis for all combinations is listed in the following Tables. Each column (except the first one) corresponds to one combination of current intensity in phase conductors 1, 2 and 3, respectively.

Table 1: *Relative deviation of MFD for a "1-2-3-0" layout*

x (mm)	*0.9-1-1*	*0.8-1-1*	*1-0.9-1*	*1-0.8-1*	*1-1-0.9*	*1-1-0.8*
20	-8%	**-14%**	-2%	-4%	1%	3%
30	-11%	**-20%**	-1%	-1%	3%	6%
40	-12%	**-23%**	0%	1%	4%	7%
50	-13%	**-24%**	0%	1%	4%	8%
60	-13%	**-25%**	0%	1%	4%	9%
80	-13%	**-26%**	0%	2%	4%	9%

Table 2: *Relative deviation of MFD for a "1-2-0-3" layout*

x (mm)	*0.9-1-1*	*0.8-1-1*	*1-0.9-1*	*1-0.8-1*	*1-1-0.9*	*1-1-0.8*
20	-5%	**-9%**	-2%	-4%	-3%	-5%
30	-5%	**-10%**	-1%	-2%	-3%	-6%
40	-5%	**-11%**	-1%	-2%	-3%	-7%
50	-6%	**-11%**	-1%	-2%	-3%	-7%
60	-6%	**-11%**	-1%	-2%	-3%	-7%
80	-6%	**-11%**	-1%	-1%	-3%	-7%

Table 3: *Relative deviation of MFD for a "1-0-2-3" layout*

x (mm)	*0.9-1-1*	*0.8-1-1*	*1-0.9-1*	*1-0.8-1*	*1-1-0.9*	*1-1-0.8*
20	-3%	-6%	-1%	-1%	-6%	**-11%**
30	-3%	-7%	0%	-1%	-6%	**-11%**
40	-4%	-7%	0%	-1%	-6%	**-11%**
50	-4%	-7%	0%	-1%	-6%	**-11%**
60	-4%	-7%	0%	-1%	-6%	**-11%**
80	-4%	-7%	0%	-1%	-6%	**-11%**

Table 4: *Relative deviation of MFD for a "0-1-2-3" layout*

x (mm)	*0.9-1-1*	*0.8-1-1*	*1-0.9-1*	*1-0.8-1*	*1-1-0.9*	*1-1-0.8*
20	1%	3%	-3%	-5%	-7%	-12%
30	3%	7%	-1%	-1%	-11%	**-20%**
40	4%	8%	0%	1%	-12%	**-23%**
50	5%	9%	0%	2%	-13%	**-25%**
60	5%	9%	0%	2%	-14%	**-26%**
80	5%	10%	0%	2%	-14%	-26%

Positive values in each Table listed above mean that the MFD in the unbalanced case is higher than in the balanced case. If the MFD in the unbalanced case is less than the MFD in the balanced case, the values are negative. Searching for the columns with the most negative values, we could find the position of the neutral conductor that would provide the lowest MFD.

Table 1 has both positive and negative values, which means that the neutral conductor located at the bottom can both decrease or increase the net MFD, depending on the amplitudes of the phase currents. The same conclusion can be obtained observing Table 4. Tables 2 and 3 contained only negative values, leading us to the conclusion that the neutral conductor located in the middle of the bus bar decreased the net MFD for any combination of current amplitudes. Columns 2 and 3 in each Table listed above correspond to unbalance, due to an amplitude deviation in line L1. It can be noticed that increasing the amplitude deviation from 10% (0.9-1-1) to 20% (0.8-1-1) the MFD relative deviation nearly doubled. The same could be said by observing columns 4 and 5, and columns 6 and 7, corresponding with the amplitude deviation in lines L2 and L3, respectively. Increasing the current unbalance further increased the MFD deviation.

3 CONCLUSIONS

The presence of current unbalance in power distribution systems is inevitable, and for that reason the analysis of its impact on the magnetic flux density distribution in the vicinity of energy bus bar systems is always reasonable.

In the balanced case the current in the neutral conductor is zero, and the magnitude of the MFD decreases more rapidly if the phase conductors are closer to each other. Therefore, in the balanced case, the best position of the neutral conductor is at the top or at the bottom of the bus bar. In unbalanced cases the magnitude of the magnetic flux density vector depends on the position of the neutral conductor, and it could be lower or higher compared to the balanced case. The lowest magnetic flux density was obtained by relocating the neutral conductor from the outside (top or bottom) in the middle of the bus bar system, in between the phase conductors.

ACKNOWLEDGMENT

This paper is supported by the Provincial Secretariat for Higher Education and Scientific Research of the Autonomous Province of Vojvodina, through the Project 142-451-3190/2023-01/01.

References

[1] Bio Initiative report: *A rationale for a biologically based public exposure standard for electromagnetic fields (ELF and RF)*, 2012. http://www.bioinitiative.org

[2] *National Research Council (US) Committee on the Possible Effects of Electromagnetic Fields on Biologic Systems*, Washington (DC): National Academies Press (US); 1997

[3] ICNIRP: *Guidelines for limiting exposure to time-varying electric and magnetic fields (1 Hz – 100 kHz)*, Health Physics, Vol. 99, Iss. 6, p.p. 818-836, 2010

[4] *Pravilnik o granicama izlaganja nejonizujućim zračenjima*, "Službeni glasnik RS", broj 104, 2009.

[5] **D. W. Deno**: *Transmission line fields*, IEEE Trans. Power App. Syst., Vol. PAS-95, no. 5, p.p. 1600-1611, 1976

[6] **R. G. Olsen, P. S. Wong**: *Characteristics of Low Frequen-cy Electric and Magnetic Fields in the Vicinity of Electric Power Lines*, IEEE Trans. Power Del., vol. 7, p.p. 2046-53, 1992

[7] IEC std 62110:2009 – *Electric and magnetic field levels generated by AC power systems – Measurement proce-dures with regard to public exposure*, 2009

[8] **J. Driesen, T. Van Craenenbroeck**: *Power Quality Application Guide: Voltage Disturbances - Intro-duction to Unbalance*, Copper Development Association, IEE Endorsed Provide, May 2002

[9] **M. Adibi, P. Milanicz, T. Volkmann**: *Asymmetry issues in power system restoration*, IEEE Trans. Power Systems, vol. 14, no. 3, p.p. 1085–91, 1997.

[10] **A. Kalyuzhny**, **G. Kushnir**: *Analysis of current unbalance in transmission systems with short lines*, IEEE Trans. Power Del., vol. 22, no. 2, p.p. 1040-48, 2007

[11] **H. Arghavani, M. Peyravi**: *Unbalanced current-based tariff*, CIRED, Session 2, p.p. 883-887, 2017

[12] **K. Ma, L. Fang, W. Kong**: *Review of Distribution Net-work Phase Unbalance: Scale, Causes, Consequences, Solutions, and Future Research Directions*, CSEE Journal of Power and Energy Systems, Vol. 6, No. 3, pp. 479-488, 2020

[13] **M. Milutinov, A. Juhas, N. Pekaric-Nadj**: *Analysis of Effects of Current Unbalance on Magnetic Field*, 17th International Symposium on Power Electronics - EE 2013, Novi Sad, Serbia, 2013

[14] **D. Antić, M. Milutinov, A. Juhas,** *Power line magnetic field deviations for three different c urrent unbalance defi-nitions*, 14th International Conference on Applied Electromagnetics - ПЕС, Niš, Serbia, pp. 1-4, 2019

[15] **K. Kasas, G. Mijatovic, D. Herceg and M. Prsa**: *Electromagnetic field distribution in vicinity of unbalanced mixed overhead power lines*, 14th International Conference on Applied Electromagnetics, ПЕС 2019, Niš, Serbia, p.p. 1-4, 2019

[16] **M. Milutinov, A. Juhas, N. Pekaric-Nadj**: *Magnetic field in vicinity of busbars with unbalanced currents*, 8th International PhD Seminar on Computational Electro-magnetics and Electromagnetic Compatibility – CEMEMC, Timisoara, Romania, 2014

[17] **M. Milutinov, A. Juhas, N. Pekarić-Nadj**: *A study on exposure to magnetic field generated by unbalanced currents*, Trans. on mathematics & Physics, Scientific Bulletin of Polytehnica University of Timisoara, vol. 60(74), no.1, p.p. 59-69, 2015

[18] **M. Milutinov, A. Juhas, N. Pekarić-Nadj**: *Relative deviation of magnetic flux density as a function of current unbalance*, 9th International PhD Seminar on Computational Electromagnetics and Bioeffects of Electromagnetic Fields, CEMBEF, Niš, Serbia, 2015

[19] **D. Antić, A. Juhas, M. Milutinov:** *Power line magnetic field deviations for three different definitions of current unbalance*, Journal of Energy Technology – JET, Vol 12, Iss 4, p.p. 61-70, 2019

[20] Web page link: https://www.eaeelectric.com/catalogs/busbar-systems/e-line-kx-busbar.pdf, last visited July 2023

Journal of Energy Technology

JET Volume 16 (2023) p.p. 23-34
Issue 3, 2023
Type of article: 1.01
http://www.fe.um.si/si/jet.htm

VALIDATION OF DISTRIBUTED ENERGY RESOURCES IN ACCORDANCE WITH VOLTAGE FLUCTUATION LIMITATIONS PRESCRIBED BY THE IEEE 1547-2018 STANDARD

VALIDACIJA RAZPRŠENIH VIROV ENERGIJE V SKLADU Z OMEJITVAMI NIHANJA NAPETOSTI, KI JIH PREDPISUJE STANDARD IEEE 1547-2018

Marko A. Dimitrijević[1]✉, Milutin Petronijević[2]

Keywords: distributed energy resources, voltage fluctuations, flicker

Abstract

The increased need for clean energy and global warming is among the biggest challenges of the modern age. One of the potential solutions to these challenges, which can be achieved by using existing technologies, are distributed energy resources (DER). DER can be an isolated system of different capacity and purpose, but, in most cases, it is connected to the electricity grid.

Connecting a DER system to the electricity grid is a complex task, the complexity in-creases with the number of integrated DERs. In order to regulate interoperability and interconnection of DERs with electricity grid, the IEEE 1547-2018 standard is imposed.

Among other requirements, the standard prescribes voltage fluctuation limitations induced by the DER. The analysis of voltage fluctuations – flicker assumes measurement procedures defined

✉ Corresponding author: Prof. Dr Marko A. Dimitrijević, Faculty of Electronic Engineering, University of Niš, Department of Electronics, Aleksandra Medvedeva 14, Niš, Serbia Tel.: +381 18 529 321, E-mail address: marko.dimitrijevic@elfak.ni.ac.rs

1 Faculty of Electronic Engineering Niš, Department of Electronics, Aleksandra Medvedeva 14

2 Faculty of Electronic Engineering Niš, Department of Energetics, Aleksandra Medvedeva 14

by IEEE 1453-2015 standard and implementation of digital flicker-meter described by IEC 61000-4-15 standard.

In this proceeding, the realization of virtual instrument for voltage fluctuation analysis will be presented. This function is part of more comprehensive system for DER validation.

Povzetek

Povečana potreba po čisti energiji in globalno segrevanje sta med največjimi izzivi sodobnega časa. Ena od možnih rešitev omenjenih izzivov, ki jo lahko dosežemo z uporabo obstoječih tehnologij, so razpršeni energetski viri (v nadaljevanju DER). DER je lahko izoliran sistem različnih zmogljivosti in za različne namene, vendar je v večini primerov priključen na elektroenergetsko omrežje. Priključitev sistema DER na elektroenergetsko omrežje je kompleksna naloga, katere kompleksnost se povečuje s številom integriranih DER. Za ureditev interoperabilnosti in medsebojnega povezovanja DER z elektroenergetskim omrežjem je uveden standard IEEE 1547-2018.

Med drugim standard predpisuje omejitev nihanja napetosti, ki jih povzročajo DER. Za analizo nihanja napetosti (flikerja) so predvideni postopki meritev, določeni v standardu IEEE 1453-2015, implementacija digitalnega flikermetra pa je opisana v standardu IEC 61000-4-15.
V članku je predstavljena realizacija virtualnega instrumenta za analizo nihanja napetosti, ki je del celovitejšega sistema za validacijo DER.

1 INTRODUCTION

Global warming caused by increased CO_2 emissions and increased demands for energy production are two related problems. In the last two decades, great efforts have been made to solve these issues. Approaches to solving it are different: from social and political – raising awareness of the need for more economical use of energy, to technical and technological – finding cleaner sources of energy and more energy efficient systems.

In the technical-technological domain, in addition to efforts to achieve stable nuclear fusion with a positive energy yield, most research is carried out in the field of renewable energy sources (RES). As nuclear fusion is currently beyond our practical reach, scientific and commercial interests are currently focused on RES, particularly photovoltaics (PV).

The first installations of PV were stand-alone power generation systems, which are located in remote areas where commercial electricity is not available, thus isolated from the public electricity grid. Nowadays, most common PV installations are systems that are connected to a public electricity grid [*1*]. Such installations are frequently named distributed energy resources (DER). However, the public electricity grid was originally designed for the delivery and consumption of electricity, but not for the generation and storage of energy at the end-user level. Therefore, the integration of DER into the public power grid represents a complex problem, which complexity increases with the number of installations and global needs for electricity. In order to regulate interoperability and interconnection of DERs with electricity grid, the IEEE 1547-2018 standard is passed.

The IEEE 1547-2018 [*2*] standard defines a number of power quality requirements, which can be divided into following categories: direct current injection and current distortion limitations, limitations of voltage fluctuations – flicker, reactive power capability and voltage/power control requirements.

In this proceeding, the part of the system for validation and testing of DER – virtual instrument for voltage fluctuation analysis is presented. The function of described virtual instrument is in compliance with IEEE 1453-2015 [*3*] standard and implementation is based on digital flicker-meter described by IEC61000-4-15 standard [*4*].

This paper is organized as follows: the concept of electrical flicker is defined and the specified standards are presented and discussed in Section 2. Section 3 describes an integrated system for DER validation with an emphasis on flicker-meter implementation. Section 4 concludes the paper.

2 THE VOLTAGE FLUCTUATIONS – FLICKER

Originally, term flicker refers to the rapid and repeated variation in light intensity. It is usually perceived as a quick and annoying fluctuation in the brightness of a light source, often at a frequency that is not easily detectable by the human eye. Flicker can be caused by various factors, and it can have several implications and effects. Most common cause of flicker is voltage fluctuation, i.e., variation in the voltage supplied to the lighting system. Typically, the term electrical flicker is synonymous with voltage fluctuations.

Apart from unpleasant visible effects, voltage fluctuations can negatively affect the operation of electronic devices. Therefore, voltage fluctuations are regulated by international and national standards to ensure the safe and stable operation of electrical systems and protect connected devices. Some of the key standards that regulate voltage fluctuations are IEEE 1453-2015 [*3*] and IEC61000-4-15 [*4*]. In order to regulate the interoperability and interconnection of DERs with the electric grid, the IEEE 1547-2018 standard [*2*] was proposed, which also prescribes limitations regarding voltage fluctuations produced by grid inverters. Some of the key limitations for voltage fluctuations specified by standards are:

- limitations for instantaneous voltage fluctuations P_{inst}, which are short term calculation of how human eye and brain respond to flickering incandescent lights,
- limitations for short-term voltage fluctuations P_{st}, which are the cumulative measure and statistical analysis of instantaneous fluctuations during ten minutes.
- limitations for long-term voltage fluctuations P_{lt}, which are voltage fluctuation occurring over two hours.

The IEEE 1547-2018 standard prescribes minimum individual DER flicker emission limits. During a one-week measurement period, in 95% of individual measurement cases, the short-term and the long-term flicker should not exceed the limits of 0.35 and 0.25, respectively.

3 THE SYSTEM FOR DER VALIDATION

The system for DER validation is aimed to facilitate testing and validation of DERs containing power electronic based grid inverters, necessary for MPPT (Maximum Power Point Tracking) and converting a DC voltage to AC voltage with standardized waveform, frequency and amplitude. The entire DER, which consists of PV panels connected in strings and arrays, a MPPT controller and a network inverter, must meet certain standards, both in terms of converted power and

in a quality of delivered electricity. In order to verify the operation in terms of fulfilling all the specific requirements prescribed by the IEEE 1547-2018 standard, it is necessary to perform a series of measurements on the DER being tested. These measurements require different instruments and different measurement setups, and in many cases, it is not possible to perform them simultaneously. For example, for a DC injection measurement one must use an ammeter with the ability to measure direct current, for measuring current harmonics an instrument for measuring the spectrum of current up to the appropriate frequency, and for voltage quality a digital flicker-meter.

In order to leverage DER validation, shorten the necessary time and reduce the costs of purchasing special instruments, this system was developed. Based on the concept of virtual instrumentation, the system uses universal modules for the acquisition of voltages and currents, while the calculations of power quality and other related parameters are performed in software on the computer. This realization concept enables the integration of several specific instruments into one unique system. Furthermore, it enables easy addition of new capabilities, as well as simple changes in functionality in accordance with future changes in standards.

Some functions of the system, related to DER verification regarding direct current injection and higher current harmonics are presented in [*5*]. Here, functions related to measuring voltage fluctuations and validating DERs against flicker will be shown.

3.1 Hardware implementation

System's hardware consists of sensors, connection circuitry and acquisition modules with computer interface. The voltages are measured directly, using National Instruments NI9225 module, equipped with three simultaneous acquisition channels, with ±300V measurement range. The resolution is 24bit, with sampling frequency is 50kHz. The module has interface that enable connection and data transfer to a computer.

3.2 Software implementation and signal analysis

Today, digital flicker-meters are used to analyze voltage fluctuations in the power grid, as well the voltage quality of grid inverters that are an integral part of DERs. The flicker-meter is designed to comply with international standards, such as IEC 61000-4-15, to accurately assess the flicker severity and provide relevant measurements. Flickermeter has three basic functions - voltage measurement, signal processing and parameter analyses, presentation and storage obtained by measurements. Here, digital flickermeter is an integral part of the system for DER testing and validation, sharing some functions such as voltage measurement/acquisition, data presentation and storage and the measurement control and management with other parts of the system. The signal processing function implies complex signal processing algorithms to analyze the voltage waveform and extract flicker parameters. These parameters, such as the instantaneous flicker (P_{inst}), short-term flicker (P_{st}) and longterm flicker (P_{lt}) are usually calculated using numerical algorithms. The virtual instrumentation-based implementation of the signal processing function, which is an integral part of the system, will be described in detail.

According to IEC 61000-4-15, the voltage fluctuation analyses virtual instrument architecture is composed of five signal processing blocks [*4*]. Some implementations of virtual instrumentation, as well as digital based flicker-meter are presented in [*6-9*].

The first block, shown in Figure 1 conditions input voltage by removing the DC component and normalizing the input voltage to output signal independent of the input voltage amplitude, maintaining constant long-term average. Voltage DC component is removed by high pass filer. The voltage normalization is performed by dividing input voltage with half-cycle RMS sliding average calculated within 1s time interval.

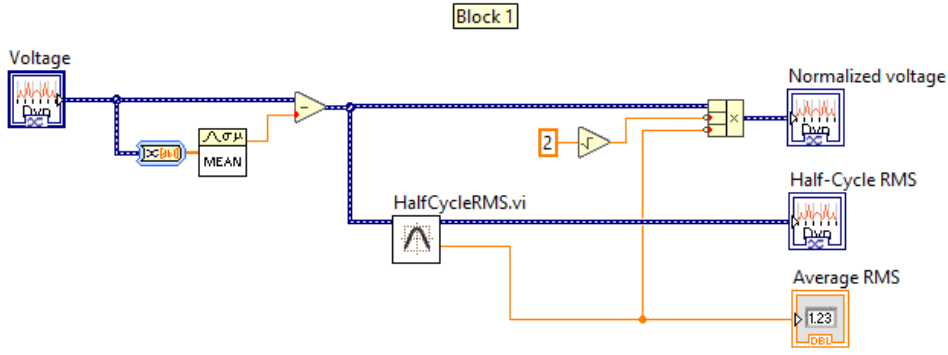

Figure 1: *First block – voltage normalization*

The input voltage is of the form

$$v_0(t) = V_{DC} + \sqrt{2}V_{rms}\left(1 + m(t)\right)\cos\omega t, \tag{3.1}$$

where V_{DC} is the DC component of input voltage, V_{rms} is the voltage RMS which is a long-term constant, $m(t)$ is the voltage fluctuation and ω the mains frequency (50Hz). Voltage fluctuations can be regarded as low-frequency amplitude modulation of an input voltage.

After removing the DC component and voltage normalization performed by half-cycle RMS average, the output of the first block is the normalized signal

$$v_1(t) = \left(1 + m(t)\right)\times\cos\omega t. \tag{3.2}$$

The second block is a square multiplier (Figure 2). The output of the second block is a signal multiplied with itself, thus, of the form

$$v_2(t) = \left(v_1(t)\right)^2 = \left(1 + 2m(t) + m^2(t)\right)\times\cos^2\omega t, \tag{3.3}$$

or by applying basic trigonometric transformations

$$v_2(t) = \frac{1}{2}\left(1 + 2m(t) + m^2(t)\right)\times\left(1 + \cos 2\omega t\right). \tag{3.4}$$

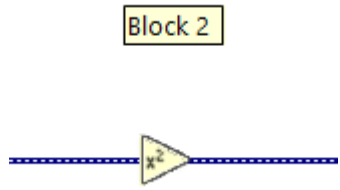

Figure 2: *Second block – square multiplier*

The third block consists of three different filters, the first two operating in combination with the square multiplier as an amplitude demodulator. The first filter is a 6th order low pass Butterworth filter, with a 3dB cutoff frequency at 35Hz. This low pass filter eliminates the double mains frequency component from the square multiplier output ($\cos 2\omega t$ term from equation (3.4)), producing a signal containing only one-time dependent term, $m(t)$. The second filter is a first order high-pass filter with a 3dB cut-off frequency at 0.05Hz, which eliminates the constant, time independent term from (1.4).

The weighting filter operates as a band-pass filter with a center frequency of 8.8Hz (Figure 3).

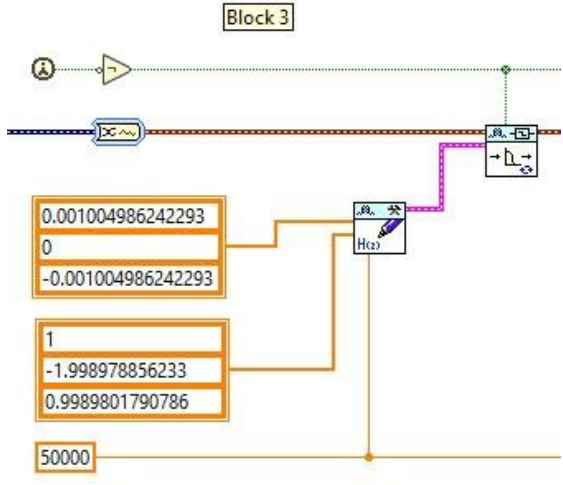

Figure 3: *The weighting filter implementation, part of the 3rd block*

The third block filter transfer function is

$$H(s)=\frac{k\omega_1 s}{s^2+2\lambda s+\omega_1^2}\times\frac{1+\frac{s}{\omega_2}}{1+\frac{s}{\omega_3}}\times\frac{1}{1+\frac{s}{\omega_4}}, \tag{3.5}$$

where *s* is the complex frequency and the filter coefficients are prescribed by IEC61000-4-15 [*4*] and given in Table 1.

Table 1: *Filter coefficients for a 50Hz mains frequency*

Parameter	Value
k	1.74802
λ	2π·4.05981
ω_1	2π·9.15494
ω_2	2π·2.27979
ω_3	2π·1.22535
ω_4	2π·21.9

The output of the third block is the modulation signal

$$m(t) = M(\omega_m) \times \cos \omega_m t, \tag{3.6}$$

which contains information of the voltage fluctuation $M(\omega_m)$ and modulation frequency ω_m. The fourth block behaves similarly to the second block with parts of the third. It consists of a squaring multiplier and a first order low-pass filter with a 300ms time constant (Figure 4).

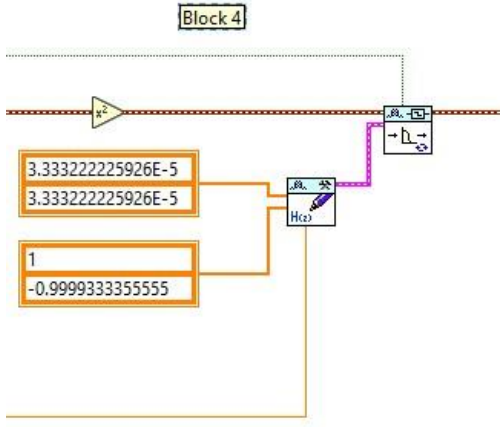

Figure 4: *The fourth block containing a squaring multiplier and first order low-pass IIR filter*

Similar to the output of the third block, the signal at the output of the fourth block has the form

$$p_{inst} \text{ » } \left(M(\omega_M)\right)^2, \tag{3.7}$$

and represents instantaneous voltage flicker, p_{inst}.

The final, fifth block (Figure 5), performs statistical analysis, providing the short-term and long-term flicker voltage fluctuation evaluations, p_{st} and p_{lt}, respectively.

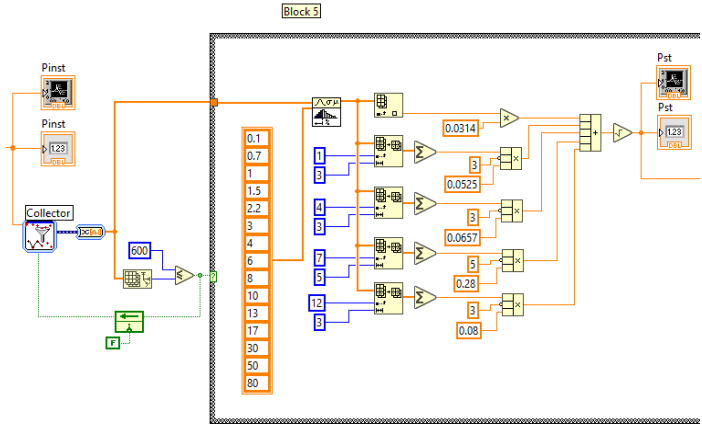

***Figure 5**: Part of the fifth block, graphic code related to the short-term flicker calculation*

The instantaneous flicker values p_{inst} are grouped over 600 second intervals, in order to perform statistical analyses. 0.1%, 1%, 3%, 10% and 50% percentiles of p_{inst} are calculated for short-term flicker evaluation. The short-term flicker is calculated as the square root of a weighted sum

$$p_{st} = \sqrt{.0314p_{0.1} + .0525p_{1s} + .0657p_{3s} + .28p_{10s} + .08p_{50s}}, \tag{3.8}$$

where index "s" in the equation suggests smoothing, i.e.

$$\begin{aligned} p_{50s} &= \frac{1}{3}\times\left(p_{30} + p_{50} + p_{80}\right) \\ p_{10s} &= \frac{1}{5}\times\left(p_{6} + p_{8} + p_{10} + p_{13} + p_{17}\right) \\ p_{3s} &= \frac{1}{3}\times\left(p_{2.2} + p_{3} + p_{4}\right) \\ p_{1s} &= \frac{1}{3}\times\left(p_{0.7} + p_{.} + p_{1.5}\right). \end{aligned} \tag{3.9}$$

The long-term voltage flicker is calculated (Figure 6) at two-hour intervals using

$$p_{lt} = \sqrt[3]{\frac{1}{12}\sum_{k=1}^{12} p_{st,k}^{3}}, \tag{3.10}$$

where $p_{st,k}$ represents the collected short time flicker values during the two-hour time interval.

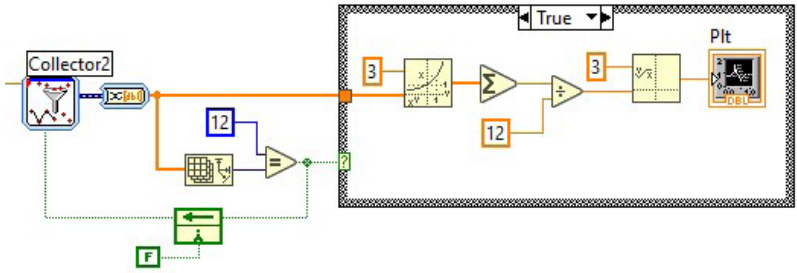

Figure 6: *The long-term flicker calculation*

4 TESTING AND VALIDATION

The implemented part of the DER testing system, which refers to the measurement of voltage fluctuations, was tested in accordance with the IEC61000-4-15 [*4*] Standard. A simulated signal, a simple periodic signal modulated by a sinusoid and a square signal were used to test this function of the system,

According to the Standard, the output of the fourth block p_{inst} must be equal to unity, with a tolerance of 8%, for appropriate voltage modulations, $m(t)$. The values averaged over 600s for sinusoidal and square modulation are given in Tables 2 and 3, respectively. Only mandatory tests were conducted. The test was performed for a 50Hz, 230V electricity grid.

Table 2: *Instantaneous flicker values for sinusoidal modulation*

Modulation frequency [Hz]	Modulation p_{inst} [%]	p_{inst}
0.5	2.325	1.041
1.5	1.067	0.933
8.8	0.25	0.932
20	0.704	1.003
25	1.037	0.993
33	2.218	1.076

Table 3: *Instantaneous flicker values for square modulation*

Modulation frequency [Hz]	Modulation $m(t)$ [%]	p_{inst}
0.5	0.509	0.920
3.5	0.342	1.059
8.8	0.196	0.965
18	0.446	0.967
21.5	0.592	1.049
22	0.612	0.929
25	0.764	1.059
25.5	0.806	0.947
28	0.915	1.009
30.5	0.847	1.056
33.3	1.671	1.035

Preliminary tests of the system function with simulated signals showed that the function of the flicker-meter was realized in accordance with the IEC61000-4-15 [*4*] Standard. Further tests are necessary in real conditions, with measured voltages and comparison with reference instruments.

5 CONCLUSION

This paper describes one function of a comprehensive, integrated and specialized DER validation system: a virtual instrument for voltage fluctuation analysis.

This implementation of the system for DER validation has a number of advantages compared to the classical approach. The described solution integrates many functions of different instruments into one system. The described function of a digital flicker-meter is one of them.

The described function of the system is tested by means of simulation. The validation is planned by means of comparison with referent instruments.

References

[1] **E. Hache, A. Palle:** *Renewable energy source integration into power networks, Research Trends and Policy Implications: A Bibliometric and Research Actors Survey Analysis*, Energy Policy, vol. 124, pp. 23-35, 2019

[2] **IEEE Standards Association:** *IEEE Std 1547-2018 (Revision of IEEE Std 1547-2003) - IEEE Standard for Interconnection and Interoperability of Distributed Energy Resources with Associated Electric Power Systems Interfaces*

[3] **IEEE Standards Association:** *IEEE Std 1453-2015 - IEEE Recommended Practice for the Analysis of Fluctuating Installations on Power Systems*

[4] **IEC:** *IEC 61000-4-15:2010 - Electromagnetic compatibility (EMC) - Part 4-15: Testing and measurement techniques - Flickermeter - Functional and design specifications*

[5] **M. Dimitrijević, M. Petronijević:** *Distributed Energy Generation System Validation According to the IEEE 1547-2018 Standard Current Distortion Limits*, 20th International Conference on Thermal Science and Engineering of Serbia - SIMTERM, pp. 107-111, 18.10.-21.10., 2022, Niš, Serbia, ISBN 978-86-6055-163-6

[6] **Drápela J., Šlezingr J.:** *A Flickermeter Based on Voltage Peak Detection Method – Part I: LabView Implementation*, In Proceedings of the 13th International Scientific Conference Electric Power Engineering, Vol. 1. Brno: Brno University of Technology. pp. 437-442

[7] **Kołek, K. et al.**: *Analysis of the practical implementation of flicker measurement coprocessor for AMI meters*, Energies 2021, 14, 1589, doi: 10.3390/en14061589

[8] **Chen Y. Y. et al.:** *A digital implementation of IEC 61000-4-15 flickermeter*, IEEE Power & Energy Society General Meeting, Denver, CO, USA, pp. 1-5, doi: 10.1109/PESGM.2015.7286254

[9] **National Instruments:** *Measuring Flickers (Electrical Power Toolkit)*, https://www.ni.com/docs/en-US/bundle/labview-electrical-power-toolkit-api-ref/page/lveptconcepts/ep_measure_flickers.html# Available: website (November 2023)

Nomenclature

(Symbols)	(Symbol meaning)
P_{inst}	Instantaneous flicker
P_{st}	Short-term flicker
P_{lt}	Long-term flicker
V_{DC}	Voltage DC component
V_{rms}	Voltage RMS value
ω	Mains angular frequency

Journal of Energy Technology

JET Volume 16 (2023) p.p. 35-44
Issue 3, 2023
Type of article: 1.01
http://www.fe.um.si/si/jet.htm

OPTIMIZATION AND ANALYSIS OF AN INTERIOR PERMANENT MAGNET SYNCHRONOUS MOTOR

OPTIMIZACIJA IN ANALIZA SINHRONSKEGA MOTORJA S POTOPLJENIMI TRAJNIMI MAGNETI

Vasilija Sarac[✉]

Keywords: Cogging torque, efficiency, interior permanent magnet motor, optimization, performance characteristics

Abstract

This paper aims to optimize an interior permanent magnet synchronous motor and analyze the operating characteristics of optimized models compared to the starting model. The optimization is done by optometric analysis, i.e., four motor parameters are selected and varied within certain boundaries, allowing new motor models to be obtained from each combination of these parameters. The best candidates are selected, i.e., models concerning the efficiency and cogging torque. The optimized models have improved efficiency and cogging torque compared to the starting model.

Povzetek

Namen članka je prikazati optimizacijo sinhronskega motorja s potopljenimi trajnimi magneti in analizirati delovne karakteristike optimiziranega modela v primerjavi z začetnim modelom. Metoda optimizacije je optometrična analiza, kar pomeni, da so izbrani štirje parametri motorja, ki se spreminjajo znotraj določenih meja, omogočajoč nove modele motorja iz kombinacij izbranih parametrov. Izbrani so najboljši kandidati, tj. najboljši modeli z vidika izkoristka in preskočno reluktančnega momenta. Optimizirani modeli imajo boljši izkoristek in preskočno reluktančni moment v primerjavi z začetnim modelom.

✉ Corresponding author: Prof. Dr. Vasilija Sarac, Goce Delcev University, Faculty of Electrical Engineering, Krste Misirkov 10-A, 2000 Stip, North Macedonia, Tel.: +389 32 550 900, E-mail address: vasilija.sarac@ugd.edu.mk

1 INTRODUCTION

Interior permanent magnet synchronous motors (IPMM) have wide applications in the electromotive industry, machine tools, and applications where high speeds are required, i.e., spindle drives. Compared to surface permanent magnet synchronous motors (SPMM) they are more robust, due to the construction of the rotor. No bandage is required to keep the magnets in place at high speeds, as the magnets are buried inside the rotor. Less magnet material is needed for the same torque density. Finally, they have good field weakening capabilities compared to SPMM, i.e., they can maintain constant power over a wide speed range, making them a good candidate for propulsion in electric cars *[1]*. The impact of various motor parameters, such as inductance per d–axis, permanent magnet flux linkage, pole pairs, and maximum current on torque-speed characteristics, has been analyzed in *[2]-[5]*. For applications in e-mobility the smooth operation of the motor is paramount. Therefore, one of the research focuses is minimizing the cogging torque. It can be achieved by optimizing the stator and rotor shape, as stated in *[6]* and *[7]*. The IPMM can be found in several topologies regarding the design of the rotor. We will name some of them: I, V, U, 2U, VV-, V, and V- topologies. Each topology has an impact on the motor`s operating characteristics (cogging torque, torque, efficiency), as it is analyzed in *[8]*, *[9]*. Besides cogging torque, efficiency is vital in motor usage and operation.

The detailed experimental study concerning the variations of the characteristics of IPMM when load, speed, and/or magnetization conditions vary, is presented in *[10]*. The optimization, i.e., the minimization of the cogging torque by Finite Element Analysis (FEA), is presented in *[11]*. The accuracy, advantages, and difficulty level of 2D and 3D FEA of IPMM are presented in *[12]*. Finding the best motor design is often a challenging, time-consuming task. Therefore, in this paper, a software module is used for designing the motor, where four parameters (the number of conductors per slot-CPS, magnet width-MW, magnet thickness-MT, and pole embrace-EMB), are varied within certain boundaries. The pole embrace has been defined as the ratio of the actual magnet arc distance in relation to the maximum possible arc distance. The cross-section of the analyzed motor is presented in Fig. 1.

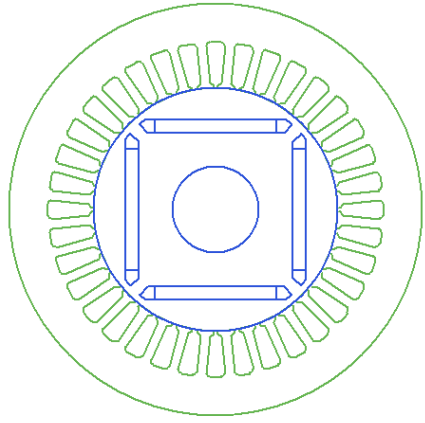

Figure 1: *Cross-section of the motor*

These four parameters' variations and combinations resulted in 840 new models. For each model, the operating characteristics are calculated: efficiency, cogging torque, weight of the magnet material, current, etc. This allows the designer to select the most optimal model in terms of several parameters, like efficiency, cogging torque, and permanent magnet consumption, thus avoiding misleading conclusions regarding the optimal design of the motor when optimization is done with optimization methods that consider only one objective function. The design gained using one objective optimization function is not always the most optimal design when other motor characteristics are analyzed. The evaluation of various motor designs that consider several operating characteristics by optometric analysis in the Ansys program allows a broader perspective of the analyzed problem, allowing the most optimal solution to be selected for several operating characteristics.

2 OPTIMIZATION

Four parameters (the number of conductors per slot-CPS, magnet width-MW, magnet thickness-MT, and pole embrace-EMB) are selected to be varied within specific ranges. The parameters are selected considering that the magnet dimensions and motor winding impact the motor efficiency and cogging torque considerably. Beside that, the magnet weight and consumption of permanent magnet material impact the motor`s price significantly, so the variation of the main magnet dimensions allows for finding the cost-effective model of the motor. The ranges of variation of parameters are presented in Table 1.

Table 1: *Ranges of variation of parameters*

Parameter	Range of variation	Step
CPS (/)	87-93	1
MT (mm)	3-7	1
MW (mm)	45-48	1
EMB (/)	0.83-0.88	0.01

The optimal designs are selected from the 840 new models derived from each combination of the four varied parameters. The first design is selected according to the highest efficiency factor, but, simultaneously, the cogging torque and magnet weight should be smaller than the initial design (BM). This design will be referred to as OM1. The second design is selected according to the smallest cogging torque, a bigger efficiency, and a smaller magnet weight than the initial design. This design will be referred to as OM2. The comparison of models BM, OM1, and OM2 is presented in Table 2. The analysis constrains all motor models to have the same output power, i.e., output torque.

Fig. 2 presents the efficiency comparison for all three models in Table II. The comparison of cogging torque for the three models is presented in Fig. 3. The air gap flux density and air-gap power for all models are presented in Fig. 4 and Fig. 5.

Table 2: *Comparison of initial and optimized models*

Parameter	BM	OM1	OM2
CPS (/)	90	90	87
MW (mm)	48	45	45
MT (mm)	5	3	3
EMB (/)	0.85	0.86	0.88
Current I_1 (A)	5.3	4.96	5.15
Stator resistance R_1 (Ω)	2.46	2.46	2.38
Wire diameter d_a (mm)	0.81	0.81	0.81
Stator slot fill factor (%)	73.4	73.4	70.97
Output power P_2 (W)	2200	2200	2200
Input power P_1(W)	2443	2414	2421
Power factor cosφ(/)	0.98	0.99	0.99
Copper losses P_{cu} (W)	208	182	189
Core losses P_{FE} (W)	13	10.2	10.2
Rated speed (rpm)	1500	1500	1500
Output torque (Nm)	14	14	14
Torque angle (degree)	54.6	67.4	68.2
Max. output power (W)	6259	4379	4474
Frictional and windage losses P_{fw} (W)	22	22	22
$M_{cogging}$ (Nm)	0.593	0.44	0.136
η (%)	90	91.1	90.9
m_{magnet} (kg)	0.84	0.47	0.47

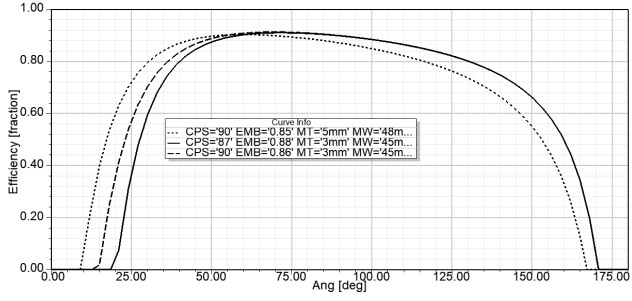

Figure 2: *Efficiency of three models*

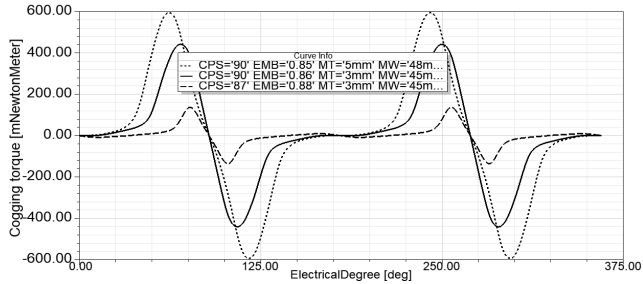

Figure 3: *Cogging torque of three models*

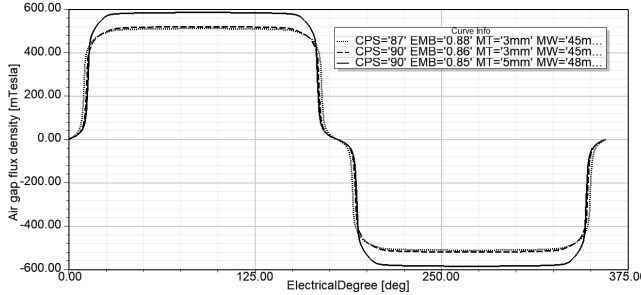

Figure 4: *Air gap flux density of three models*

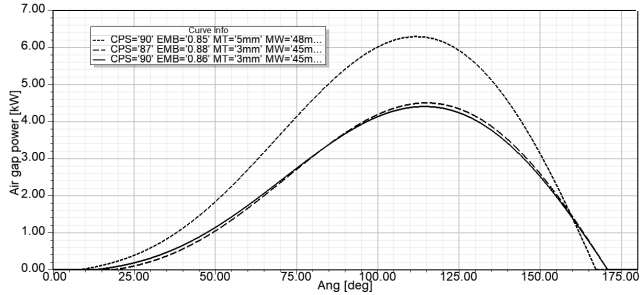

Figure 5: *Air gap power of three models*

The motor analysis proceeds with FEA to determine the motor cross-section's magnetic flux density. The FEA determines the areas of the motor core where saturation occurs, thus providing valuable data for the motor designers. The flux density distribution for all models for the rated load operating conditions is presented in Fig. 6.

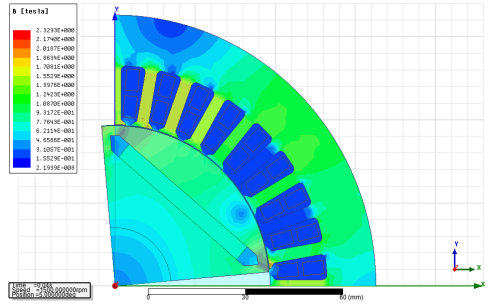

(a) BM

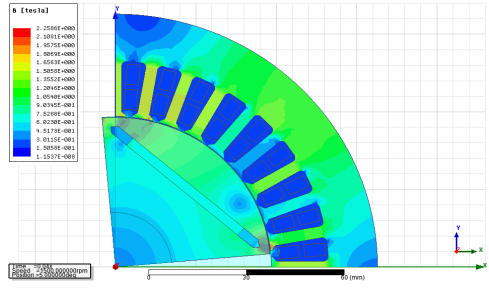

(b) OM1

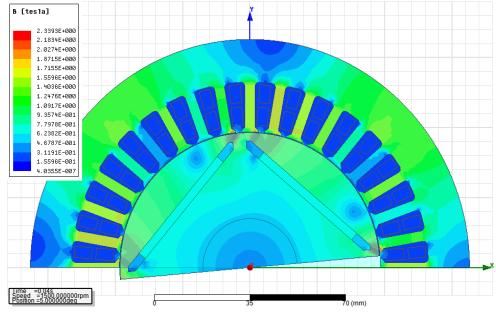

(c) OM2

Figure 6: *Flux density distribution of three models*

3 DISCUSSION OF RESULTS

The design process of electrical machines involves various parameters regarding the electrical, magnetic, and geometric properties of the analyzed design. The ultimate goal of designers is to achieve the most optimal solution for the machine regarding several objective optimization functions with minimum costs. By varying the four parameters of IPMM, the numerous combinations, i.e., 840 combinations, are obtained from these four varied parameters, which define the new motor models. For each new model several operating characteristics are calculated simultaneously, according to which the goodness of the design is estimated. The advantage of the parametric analysis is that each model can be evaluated according to several

operating characteristics that are calculated simultaneously and compared directly. The analysis aims to achieve high efficiency, minimum cogging torque, and small consumption of permanent magnet material. According to the results presented in Table 2, two models satisfy the above mentioned criteria. The model OM1 had the biggest efficiency of all models, but relatively big cogging torque. However, this design has considerably better characteristics than the starting model BM. Model OM2 had slightly decreased efficiency compared to OM1, due to the increased current and the copper losses compared to OM1, but considerably decreased cogging torque. Also, the permanent magnet's weight was reduced considerably compared to the BM, which reduces the overall costs for the motor construction. As the difference in efficiency between models OM1 and OM2 was negligible, model OM2 is the best candidate for the optimized model of BM. Therefore, the impact of each of the varied parameters on motor efficiency and cogging torque for OM2 is presented in Figs. 7 and 8 correspondingly. In the results presented in Figs. 7 and 8, the impact was analyzed of one varied parameter on efficiency and cogging torque. In contrast, the other three parameters were kept constant and equal to the values presented in Table 2.

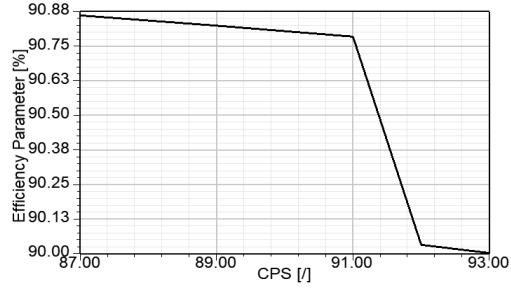

(a) Impact of CPS

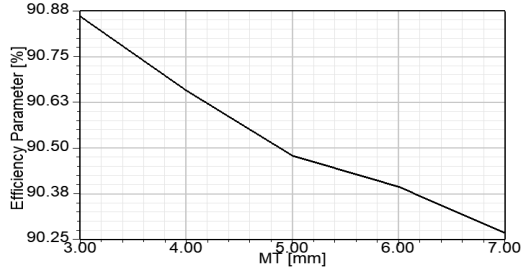

(b) Impact of MT

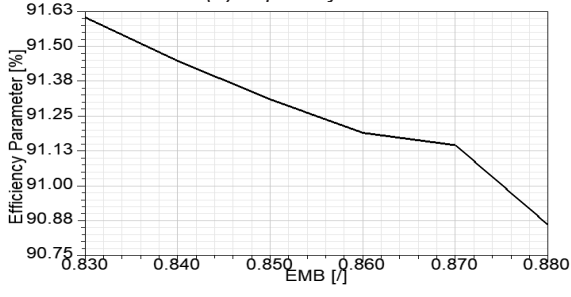

(c) Impact of EMB

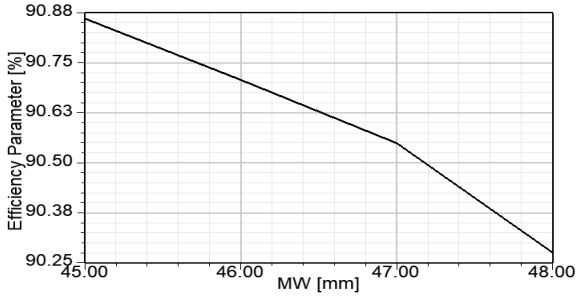

(d) Impact of MW

Figure 7: *The impact of varied parameters on motor efficiency*

From the results presented in Fig.7a) it can be concluded that the increase in the number of CPS decreases the efficiency. This is due to the increased resistance, which increases the copper losses. The decrease in efficiency is not linear, as the slot fill factor is set to a limited value of 75 %, so the cross-section of the copper wire is adjusted automatically when the limit of the slot fill factor is reached, which changes the stator phase resistance. The increase in the amount of magnet material, according to Figs. 7 b), c), and d) decreases the motor efficiency.

On the other hand, according to Fig. 8 c), the increase in pole embrace impacts decreasing the cogging torque significantly. Increasing magnet width and thickness increases the cogging torque (Figs. 8a) and b). The number of conductors per slot does not impact the cogging torque (Fig. 8 d).

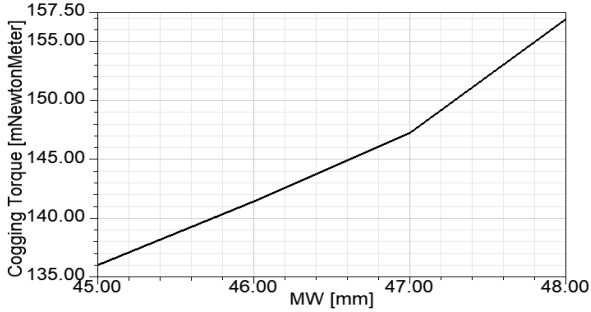

(a) impact of MW

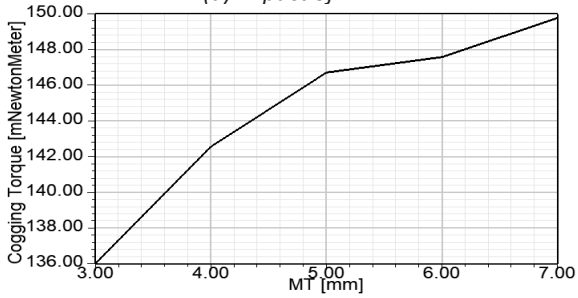

(b) impact of MT

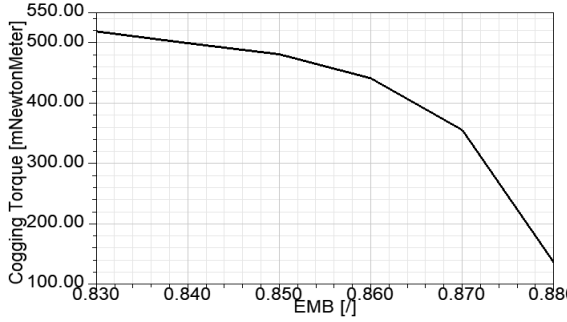

(c) impact of EMB

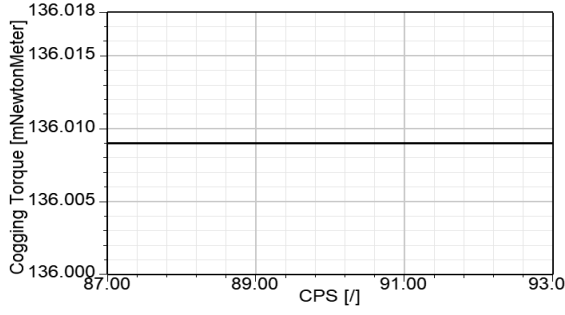

(d) impact of CPS

Figure 8: *The impact of varied parameters on cogging torque*

Fig. 6 shows that all three models were designed well, and no significant core saturation was detected. The very small parts of the stator teeth are saturated, but, generally, the flux density distribution is within the expected limits in the stator yoke, teeth and rotor core. Samarium cobalt magnets were used in all models, and, according to Fig. 6, no demagnetization of the magnets should occur.4

CONCLUSION

Energy efficiency and green technologies have become some of the most important goals of the modern society. Considering that more than the half of world-wide consumption of electricity is attributed to electrical motors, their efficiency is one of the key parameters in the design, manufacturing and usage of motors. The usage of electrical motors is extended in transportation systems, where the comfort of the passengers is of paramount importance. It is expected that the motor will operate smoothly without noise and vibrations, often present, when there is a large cogging torque. Therefore, this paper analyzes and optimizes the synchronous motor with internal magnets with respect to the efficiency and cogging torque. The most optimal combination of conductors per slot, magnet width, magnet thickness, and position of the magnets from the rotor surface is selected, resulting in a model with increased efficiency, decreased cogging torque, and magnet mass.

References

[1] **A. Dalcali**: *Optimal design of high-performance interior PM motor for electrical vehicle*, The International Journal of Energy & engineering science, Vol. 3, Iss.2, p.p. 26-35, 2018

[2] **Y. E. Shklyarskiy, A. Y. Shklyarskiy, A. S. Lutonin:** *Sizing parameters of interior permanent magnet synchronous motor based on torque-speed characteristics*, Journal of Physics: Conference Series, 1753 012026, 2021.

[3] **E.S. Beser**: *Electrical equivalent circuit for modelling permanent magnet synchronous motor*, Journal of Electrical Engineering, Vol.72, Iss.3, p.p. 176-183, 2021

[4] **B.-W. Jo, J.-K. Kang, C.-H. Song, K.-C. Kim:** *Electromagnetic Characteristics Analysis of the Interior Permanent Magnet Synchronous Motor considering Temperature Change*, International Journal of Engineering & Technology, Vol. 7 , Iss. 3.24, p.p. 194-196, 2018

[5] **M. Künzler, R. Pfüger, R. Lehmann, Q. Werner:** *Dimensioning of a permanent magnet synchronous machine for electric vehicles according to performance and integration requirements,* Automotive and Engine Technology Vol. 7, p.p. 97–104, 2022

[6] **J.-S. Yu, H.-W. Cho, J.-Y. Choi, S.-M. Jang, S.-H Lee:** *Optimum Design of Stator and Rotor Shape for Cogging Torque Reduction in Interior Permanent Magnet Synchronous Motors*, Journal of Power Electronics, Vol. 13, Iss. 4, pp. 546-551, 2013

[7] **S.-e. Kim, Y.-m. You***: Optimization of a Permanent Magnet Synchronous Motor for e-Mobility Using Metamodels*, Applied Sciences, Vol. 12, Iss.3, 1625, 2022

[8] **B. M. Dinh, N. V. Anh:** *Detail Design of Interior Permanent Magnet Motor for Electric Vehicle*, Proceedings of the International Conference on Industrial Engineering and Operations Management Istanbul, Turkey, March 7-10, p.p. 1329-1336, 2022

[9] **L. Niu, M. Zhang:** *The optimal design and research of interior permanent magnet synchronous motors for electric vehicle applications*, The Journal of Engineering, 2023:e12258, p.p. 1-20, 2023

[10] **M. Caruso, A. O. Di Tommaso, R. Miceli, C. Nevoloso, C. Spataro, F. Viola:** *Characterization of interior permanent magnet synchronous motors for loss model algorithm identification*, 19th International Workshop on ADC Modelling and Testing , Budapest, Hungary, p.p. 37-42, 2016

[11] **G. Zhang, We. Yu , W. Hua, R. Cao, H. Qiu, A. Guo:** *The Design and Optimization of an Interior, Permanent Magnet Synchronous Machine Applied in an Electric Traction Vehicle Requiring a Low Torque Ripple*, Applied Science, Vol. 9, Iss. 17, 3634, 2019

[12] **S. Naik, B. Bag, K. Chandrasekaran:** *A 2D and 3D Analysis on Electromagnetic Parameters of Spoke-shape Interior Permanent Magnet Synchronous Motor Using FEM*, Periodica Polytechnica Electrical Engineering and Computer Science, Vol. 67, Iss.2, p.p. 181–193, 2023

Journal of Energy Technology

JET Volume 16 (2023) p.p. 45-52
Issue 3, 2023
Type of article: 1.01
http://www.fe.um.si/si/jet.htm

AN APPROXIMATE MODEL FOR DETERMINING THE RESISTANCE OF A HEMISPHERICAL GROUND ELECTRODE PLACED AT THE TOP OF A NON-HOMOGENEOUS TRUNCATED CONE

PRIBLIŽNI MODEL ZA DOLOČANJE UPORA POLOKROGLE OZEMLJENE ELEKTRODE, NAMEŠČENE NA VRH NEHOMOGENEGA PRISEKANEGA STOŽCA

Dragan Vučković[1✉], Dejan Jovanović[2], Nenad Cvetković[2], Miodrag Stojanović[1], Dragan Tasić[1]

Keywords: Estimation method, grounding system, non-homogeneous soil, resistance, hemispherical electrode

Abstract

The procedure for analysis of a hemispherical ground electrode placed at the top of a hill is presented in the paper. The mountain is modelled as a truncated cone of finite height consisting of two homogeneous areas, each having different electrical characteristics. The applied approach is a combination of several recently proposed procedures. It includes the application of the Estimation method and the use of an approximate expression in closed form. The obtained results are validated and compared with those obtained using the COMSOL program package.

✉ Corresponding author: M.Sc Dragan Vučković, University of Nis, Faculty of Electronic Engineering, Department of Power Engineering, A. Medvedeva 14, 18000 Nis, Serbia, Tel.: +381 18 529 305, E-mail address: dragan.vuckovic@elfak.ni.ac.rs

1 University of Nis, Faculty of Electronic Engineering, Department of Power Engineering, A. Medvedeva 14, 18000 Nis, Serbia

2 University of Nis, Faculty of Electronic Engineering, Department of Theoretical Electrical Engineering, A. Medvedeva 14, 18000 Nis, Serbia

Povzetek

V prispevku je predstavljen postopek analize polkrogle ozemljitvene elektrode, nameščene na vrhu hriba. Gora je modelirana kot prisekan stožec končne višine, sestavljen iz dveh homogenih območij, od katerih ima vsako različne električne značilnosti. Uporabljeni pristop je kombinacija več nedavno predlaganih postopkov. Vključuje uporabo metode ocenjevanja in uporabo približnega izraza v zaprti obliki. Dobljene rezultate smo validirali in primerjali z rezultati, pridobljenimi s programskim paketom COMSOL.

1 INTRODUCTION

The most important feature of the grounding electrode, the resistance value, is conditioned by electrode geometry, conductor characteristics, soil structure and the physical shape of the surrounding ground. Various procedures are based on different numerical and semi-numerical methods, depending on the soil structure and corresponding geometrical model. For example, in *[1-2],* the ground is modelled as a homogeneous half space of a flat surface. Very often, the non-homogeneous ground is modelled as multi-layered *[3-4]*, sectoral *[5]*, a semi-spherically *[6-7]* or semi-cylindrically shaped domain *[8]*.

The problem of determining the resistance of a hemispherical ground electrode placed at the top of a non-homogeneous truncated cone modelled with three homogeneous domains having different electrical characteristics is investigated in this paper. The procedure applied in this paper is based on approaches from *[9-11]*. The procedure for analysis of a hemispherical ground electrode placed at the top of a hill was proposed in *[9]*. This approach was improved in *[10]* by assuming current density distribution in two different forms, depending on the observed domain. The method applied in this paper is an extended application of the approach based on procedures from *[9-10]* and presented in *[11]*. The previously mentioned approach offers the possibility of modelling a truncated cone as a non-homogeneous domain consisting of different homogeneous areas.

The applied procedure does not require integration, and all the used approximate expressions are given in closed form. The COMSOL program package based on the Finite Element Method was used to validate the obtained results.

2 PROBLEM DESCRIPTION

The hemispherical ground electrode is placed at the top of a non-homogeneous truncated cone consisting of three homogeneous domains having specific conductivities σ_1, σ_3 and σ_3 respectively. The boundary surfaces between the domains are flat.

The radius of the electrode is r_1 and the cone base radius is d_1. The depth of the boundary surfaces is labelled with d_1, and the cone slope is defined with angle α. In this paper, the proposed solution for the structure from Fig. 1 is based, as has already been emphasised, on the approaches from *[9-11]*. However, the chosen model of a non-homogeneous truncated cone is a more complex structure related to those from *[9-11]*. One could expect that, in general, the case ground structure is non-homogeneous, and therefore, the model from Figure 1 can be used for approximating ground non-homogeneity.

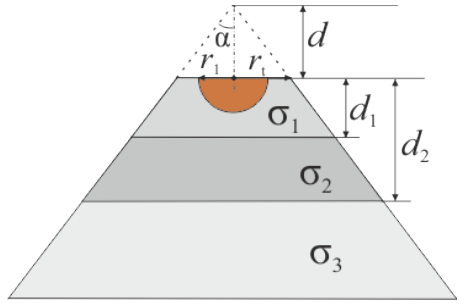

Figure 1: *The hemispherical ground electrode and truncated cone approximated with three homogeneous domains (flat boundary surface).*

3 PROCEDURE DESCRIPTION

The procedure for determination of the resistance of hemispherical ground electrode placed at the top of the truncated cone approximated with three homogeneous domains (Figure 2) will be derived, in order to generate the procedure for determination of the approximate resistance of the electrode from Figure 1. It is based on the approaches proposed in *[11]*. The boundary surfaces between domains are calotte surfaces having the radii r_3 and r_3, and the rest of the geometry parameters can be seen in Figure 2.

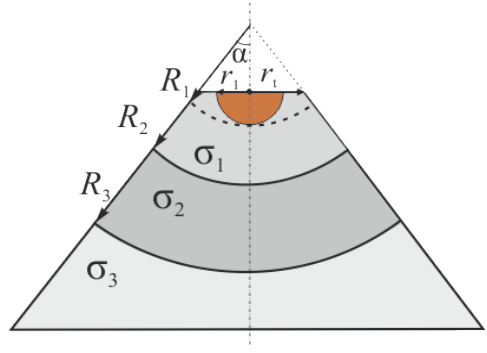

Figure 2: *The hemispherical ground electrode and truncated cone approximated with three homogeneous domains (oval boundary surface).*

Based on the procedure described in *[11]*, the current densities in the cone domain can be expressed as,

$$\vec{J}_1 = \frac{I}{2\pi r^2}\hat{r},\ r_1 < r < r_t \ \text{, and} \tag{3.1a}$$

$$\vec{J}_2 = \frac{I}{2\pi\left(1-\cos\alpha\right)R^2}\hat{R},\ R_1 < R < \infty \tag{3.1b}$$

In previous expressions, r is a radial coordinate, while $\hat{r}$ is the corresponding spot of the coordinate system having origin at the middle point of the upper surface of the truncated cone. Similarly, $\hat{R}$ and $\hat{R}$ are the radial coordinate and corresponding spot of the coordinate system having origin at the imaginary top point of the cone *[11]*.

Using a local form of Ohm's law, for the electric field is obtained,

$$\vec{E}_{11} = \frac{\vec{J}_1}{\sigma_1} = \frac{I}{2\pi\sigma_1 r^2}\hat{r},\ r_1 < r < r_t \tag{3.2a}$$

$$\vec{E}_{12} = \frac{\vec{J}_2}{\sigma_1} = \frac{I}{2\pi\sigma_1 (1-\cos\alpha) R^2}\hat{R},\ R_1 < R < R_2 \tag{3.2b}$$

$$\vec{E}_2 = \frac{\vec{J}_2}{\sigma_2} = \frac{I}{2\pi\sigma_2 (1-\cos\alpha) R^2}\hat{R},\ R_2 < R < R_3 \tag{3.2c}$$

$$\vec{E}_3 = \frac{\vec{J}_2}{\sigma_3} = \frac{I}{2\pi\sigma_3 (1-\cos\alpha) R^2}\hat{R},\ R_3 < R < \infty \tag{3.2d}$$

The potential φ_s of the electrode surface from Fig 2 can be determined approximately as *[9, 12]*,

$$\varphi_s = \int_{r_1}^{r_t} E_{11}\,\mathrm{d}\,r + \int_{R_1}^{R_2} E_{12}\,\mathrm{d}\,r \int_{R_2}^{R_3} E_2\,\mathrm{d}\,R + \int_{R_3}^{\infty} E_3\,\mathrm{d}\,R \tag{3.3}$$

Now, for the potential φ_s obtains,

$$\varphi_s = \frac{I}{2\pi\sigma_1}\left[\frac{1}{r_1} - \frac{1}{r_t} + \frac{1}{(1-\cos\alpha)}\left(\frac{1}{R_1} - \frac{1}{R_2}\right)\right] + \frac{I}{2\pi\sigma_2}\frac{1}{(1-\cos\alpha)}\left(\frac{1}{R_1} - \frac{1}{R_2}\right) + \\ + \frac{I}{2\pi\sigma_3}\frac{1}{(1-\cos\alpha)}\frac{1}{R_3}. \tag{3.4}$$

The electrode resistance value is

$$R_g = \frac{\varphi_s}{I} = \frac{1}{2\pi\sigma_1}\left[\frac{1}{r_1} - \frac{1}{r_t} + \frac{1}{(1-\cos\alpha)}\left(\frac{1}{R_1} - \frac{1}{R_2}\right)\right] + \\ + \frac{1}{2\pi\sigma_2}\frac{1}{(1-\cos\alpha)}\left(\frac{1}{R_1} - \frac{1}{R_2}\right) + \frac{1}{2\pi\sigma_3}\frac{1}{(1-\cos\alpha)}\frac{1}{R_3}. \tag{3.5}$$

There is interest to emphasise that in the previous expression

$$R_1 = \frac{r_t}{\tan\alpha} + r_1 \tag{3.6}$$

4 ESTIMATION METHOD

In order to use the previously described procedure for the determination of the approximate resistance of the hemispherical grounding electrode from Figure 1, the Estimation method is introduced into the procedure.

From Figure 3 can be noticed the upper (R_{2e} , R_{3e}) and lower (R_{3i} , R_{3i}) values of the boundary surface radii. The approximate resistance of the system can be determined as the arithmetic mean of the resistance values calculated for the upper and lower radii values.

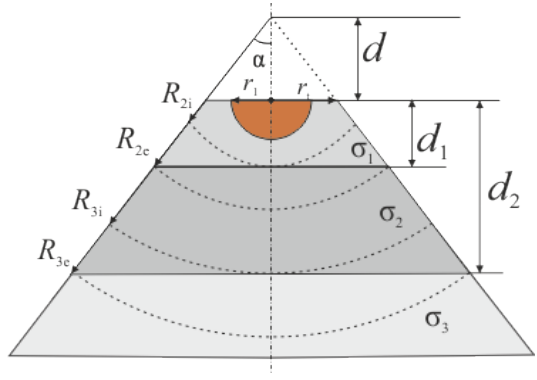

Figure 3: *Estimation method application.*

The geometrical parameters from Figure 3 can be determined as

$$d = r_t \cot\alpha, R_{2i} = d + d_1, R_{2e} = \frac{d + d_1}{\cos\alpha}, \qquad R_{3i} = d + d_2, R_{3e} = \frac{d + d_2}{\cos\alpha}. \tag{4.1}$$

Now, after determination of the resistance values for $R_2 = R_{2i}$, $R_3 = R_{3i}$ (labels as R_{gi}), i.e. for $R_2 = R_{2e}$, $R_3 = R_{3e}$ (labelled as R_{ge}), the approximate value of the grounding electrode resistance can be determined as the arithmetic mean

$$R_g = \frac{R_{2e} + R_{2i}}{2} \text{ , i.e.} \tag{4.2a}$$

$$R_g = \frac{1}{2\pi\sigma_1}\left(\frac{1}{r_1} - \frac{1}{r_t}\right) + \frac{1}{2\pi\sigma_1(1-\cos\alpha)}\left(\frac{1}{r_t + d} - \frac{R_{2e} + R_{2i}}{2R_{2e}R_{2i}}\right) + \\ + \frac{1}{2\pi\sigma_2(1-\cos\alpha)}\left(\frac{R_{2e} + R_{2i}}{Rr_{2e}R_{2i}} - \frac{R_{3e} + R_{3i}}{2R_{3e}R_{3i}}\right) + \frac{1}{2\pi\sigma_3(1-\cos\alpha)}\frac{R_{3e} + R_{3i}}{2R_{3e}R_{3i}}. \tag{4.2b}$$

5 NUMERICAL RESULTS

The obtained results and relative errors obtained by the described method are shown in Table 1 for $\{\sigma_2/\sigma_1 = 5, \sigma_3/\sigma_1 = 10\}$ and Table 2 for $\{\sigma_2/\sigma_1 = 5, \sigma_3/\sigma_1 = 10\}$.

The set of other parameters` values is $\sigma_1 = 0.001\text{S/m}$, $d_1 = 10\,\text{m}$, $d_1 = 10\,\text{m}$, $\alpha \in \{45^0, 50^0, 55^0, 60^0\}$ and $r_t \in \{10\,\text{m}, 20\,\text{m}\}$.

The values of the parameters have been selected based on *[11]*. The obtained results ($R_{g\,ap}$) were validated with the values obtained from the COMSOL program package application (R_g).

From the results shown in Tables 1-2, one can conclude that the relative error was not larger than 15,4%, which can be assumed as a satisfactory result. A more detailed analysis requires a more extensive data set, but at this research level, it can be indicated that the proposed simple approach can be assumed as valuable and applicable in practice.

***Table 1*:** Grounding resistance for $\sigma_1 = 0.001\text{S/m}$, $r_1 = 5\,\text{m}$, $d_1 = 10\,\text{m}$, $d_2 = 20\,\text{m}$, $\sigma_2/\sigma_1 = 5$ *and* $\sigma_3/\sigma_1 = 10$

α=45^0			
r_t[m]	$R_{g\,ap}$ [Ω]	R_g[Ω]	Relative error [%]
10	22,2134	24,066	7,697997
20	23,5436	22,348	5,349919
α=50^0			
r_t[m]	$R_{g\,ap}$ [Ω]	R_g[Ω]	Relative error [%]
10	22,2324	23,735	6,330735
20	23,6881	22,327	6,096206
α=55^0			
r_t[m]	$R_{g\,ap}$ [Ω]	R_g[Ω]	Relative error [%]
10	22,3231	23,445	4,785242
20	23,8392	22,310	6,854325
α=60^0			
r_t[m]	$R_{g\,ap}$ [Ω]	R_g[Ω]	Relative error [%]
10	22,4740	23,198	3,120959
20	23,9916	22,295	7,609778

Table 2: *Grounding resistance for* $\sigma_1 = 0.001\text{S/m}$, $r_1 = 5\,\text{m}$, $d_1 = 10\,\text{m}$, $d_2 = 20\,\text{m}$, $\sigma_2/\sigma_1 = 10$ *and* $\sigma_3/\sigma_1 = 50$.

$\alpha=45^0$			
r_t[m]	$R_{g\,ap}$ [Ω]	R_g[Ω]	Relative error [%]
10	20,3582	24,066	15,4068
20	22,3068	22,348	0,184357
$\alpha=50^0$			
r_t[m]	$R_{g\,ap}$ [Ω]	R_g[Ω]	Relative error [%]
10	20,6405	23,735	13,03771
20	22,5950	22,327	1,20034
$\alpha=55^0$			
r_t[m]	$R_{g\,ap}$ [Ω]	R_g[Ω]	Relative error [%]
10	20,9414	23,445	10,67861
20	22,8605	22,310	2,467503
$\alpha=60^0$			
r_t[m]	$R_{g\,ap}$ [Ω]	R_g[Ω]	Relative error [%]
10	21,2632	23,198	8,340374
20	23,1052	22,294	3,638647

6 CONCLUSIONS

The procedure, based on several recently proposed approaches for approximate determination of the resistance value of a hemispherical ground electrode placed at the top of the truncated cone, is presented in the paper. The obtained results indicate that this simple approach can be used for approximating the described ground non-homogeneity.

ACKNOWLEDGEMENTS

The research described in the paper was partially supported by the Ministry of Science, Technological Development and Innovation of the Republic of Serbia.

References

[1] **T. Takashima, T. Nakae, R. Ishibahsi:** *High frequency characteristics of impedances to ground and field distributions of ground electrodes*, IEEE Transactions on Power Apparatus and Systems, Vol. 9, pp. 1893-1900, 1980. Available: https://doi.org/10.1109/MPER.1981.5511414 (04.12.2023)

[2] **R. J. Heppe:** *Step Potential and body currents near grounds in two-layer earth*, IEEE Transactions on Power Apparatus and Systems, Vol. 98, pp. 45-59,1979. Available: https://doi.org/10.1109/TPAS.1979.319512 (04.12.2023)

[3] **P. D. Rancic, L. V. Stefanovic, Dj. R. Djordjevic:** *A new model of the vertical ground rod in two-layer earth*, IEEE Transaction on Magnetics, Vol. 28, pp. 1497-1500, 1992. Available: https://doi.org/10.1109/20.123980 (04.12.2023)

[4] **P. D. Rancic, L. V. Stefanovic, Dj. R. Djordjevic:** *An improved linear grounding system analysis in two-layer earth*, IEEE Transaction on Magnetics, Vol. 32, pp. 5179-5187, 1996. Available: https://doi.org/10.1109/20.538620 (04.12.2023)

[5] **P. D. Rancic, Z. P. Stajic, Dj. R. Djordjevic, B. S. Tosic:** *Analysis of linear ground electrodes placed in vertical three-layer earth*, IEEE Transaction on Magnetics, Vol. 32, pp. 1505-1508, 1996. Available: https://doi.org/10.1109/20.497535 (04.12.2023)

[6] **N. N. Cvetkovic, P. D. Rancic:** *A simple model for a numerical determination of electrical characteristics of a pillar foundation grounding system*, Engineering Analysis with Boundary Elements, Elsevier, Vol. 33, pp. 555-560, 2009**.** Available: https://doi.org/10.1016/j.enganabound.2008.08.005 (04.12.2023)

[7] **N. N. Cvetkovic, P. D. Rancic:** *Influence of Foundation on Pillar Grounding System's Characteristics*, COMPEL: The International Journal for Computation and Mathematics in Electrical and Electronic Engineering, Vol. 28, pp. 471-492, 2009. Available: https://doi.org/10.1108/03321640910929335 (04.12.2023)

[8] **D. D. Vuckovic, N. N. Cvetkovic, M. S. Stojanovic, I. Iatcheva:** *Approximate model for ground inhomogeneity with rectangular cross-section: application to analysis of grounding systems*, Electrical Engineering, Springer, Vol. 100, pp. 75-82, 2018. Available: https://doi.org/10.1007/s00202-016-0483-1 (04.12.2023)

[9] **A. Sunjerga, F. Rachidi, M. Rubinstein, D. Poljak:** *Calculation of the grounding resistance of structures located on elevated terrain*, IEEE Transactions on Electromagnetic Compatibility, Vol. 61, pp. 1891-1895, 2019. Available: https://doi.org/10.1109/TEMC.2018.2877214 (04.12.2023)

[10] **K. B. Tan, H. M. Lu, Y. Zhang, W. C. Zuo:** *Analysis of the grounding resistance of a hemispheric electrode located on a truncated cone*, IEEE Transactions on Electromagnetic Compatibility, Vol. 62, pp. 1361-1363, 2020. Available: https://doi.org/10.1109/TEMC.2019.2940902 (04.12.2023)

[11] **D. Vuckovic, D. Jovanovic, N. Cvetkovic, D. Tasic, K. Kasas-Lazetic:** *An approximate model for determining the resistance of a hemispherical ground electrode placed on a non-homogeneous truncated cone*, Acta Polytechnica Hungarica, Vol. 20, pp. 119-133, 2023. Available**:** https://doi.org/10.12700/APH.20.6.2023.6.7 (04.12.2023)

JET Journal of Energy Technology

JET Volume 16 (2023) p.p. 53-60
Issue 3, 2023
Type of article: 1.01
http://www.fe.um.si/si/jet.htm

ROBOTIC SANDING OF FREESTANDING BATHTUBS

ROBOTSKO BRUŠENJE PROSTOSTOJEČIH KADI

Antonio Petrčić[1], Toni Kralj [2], Tihomir Mihalić [3], Nikola Šimunić[✉]

Keywords: industrial manipulator, sanding, automatic force detection

Abstract

Modern production is characterized by great variability, with the possibility of making complex parts. However, as modern technology helps increase the efficiency of factors of production, it can also replace labour to reduce costs. For example, Artificial Intelligence and robotic systems are used in manufacturing, to achieve greater productivity and reduce costly human errors. That is why human resources are being replaced gradually by automated robotic systems. In this paper a novel approach was used to sand and polish freestanding bathtubs, using an industrial manipulator and a standardised procedure of sanding, with automatic detection of force when in contact with a part. This process resulted in over 30% of savings in consumable materials (sand paper, etc.) and an almost 50% increase in productivity. To conclude, using two robotic cells in the process of manufacturing of freestanding bathtubs produced four times greater labor saving in comparison to manual sanding.

Povzetek

Za sodobno proizvodnjo je značilna velika variabilnost z možnostjo izdelave kompleksnih delov. Sodobna tehnologija pomaga povečati učinkovitost proizvodnih dejavnikov, posledično lahko tudi zmanjša stroške. Na primer, umetna inteligenca in robotski sistemi se uporabljajo v proizvodnji za doseganje večje produktivnosti in zmanjšanje dragih človeških napak. Zato človeške vire postopoma nadomeščajo avtomatizirani robotski sistemi. V tem prispevku je bil uporabljen

✉ Corresponding author: Dr. Sc. Nikola Šimunić, Tel.: +385 (0)91 2447 202, Mailing address: Karlovac University of Applied Sciences, I. Meštrovića 10, 47000 Karlovac, Croatia, E-mail address: nsimunic@vuka.hr

1 Karlovac University of Applied Sciences, Mechanical Engineering Department, I. Meštrovića 10, 47000 Karlovac

2 Karlovac University of Applied Sciences, Mechanical Engineering Department, I. Meštrovića 10, 47000 Karlovac

3 Tehničko veleučilište Zagreb, Mechanical Engineering Department, Vrbik 8, 10 000 Zagreb

nov pristop za brušenje in poliranje samostoječih kadi z uporabo industrijskega manipulatorja in standardiziranega postopka brušenja s samodejnim zaznavanjem sile ob stiku z delom. Rezultat tega postopka je več kot 30-odstotni prihranek pri potrošnem materialu (brusni papir itd.) in skoraj 50-odstotno povečanje produktivnosti. Če sklenemo, z uporabo dveh robotskih celic v procesu izdelave prostostoječih kopalnih kadi smo dosegli štirikrat večji prihranek dela v primerjavi z ročnim brušenjem.

1 INTRODUCTION

The idea of automatic devices that serve man has been around for a long time, like the idea of automatic door opening recorded in historical stories. Around the 9th century, hundreds of preserved texts and ideas were collected and compiled into one book called “The Science of Ingenious Mechanisms”. This book and the Renaissance brought together many scientists, including Leonardo da Vinci, to create or design some of the first automated devices. The industrial revolution brought with it an increasing demand for production, and thus the motivation to automate systems. The development of the integrated circuit, the invention of numerically controlled (NC) machines, and the popularity of computers, helped create the first simple industrial robot. They managed to replace people in performing difficult and monotonous jobs. However, they did not have as many sensors as today’s robots have, so they were used only for the simplest tasks, such as accepting an object and placing it in a certain position [1].

An industrial robot is a mechanical device that is controlled automatically, and is adaptable enough to be programmed to perform various tasks and be able to use various tools. As electronics, sensors and computing progressed, so did the capabilities of industrial robots, which performed increasingly complex tasks, such as welding, assembly, packaging, all achieved with precision, speed and repeatability [1].

Figure 1 [2]. shows an estimate of the number of industrial robots installed annually in the world. From 2007 to 2009, a drastic drop can be observed in the number of robots, due to the global financial crisis, and stagnation in 2020 due to the impact of COVID-19.. The next decade was characterized by a significant growth of industrial robotics.

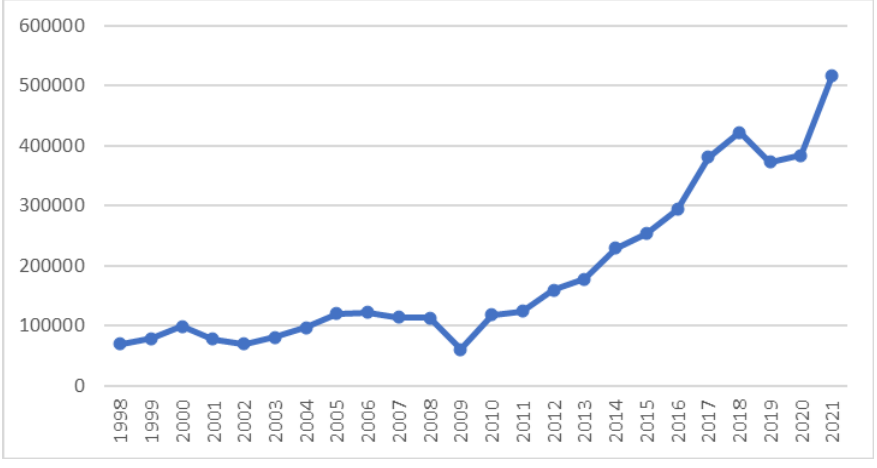

Figure 1: *Estimate of the number of robots installed annually in the world*

1 SANDING PROCES

According to DIN 8580, sanding belongs to the machining processes of particle separation with a cutting tool with a geometrically undefined cutting edge, together with super-finishing, honing and lapping. Sanding is the most common and cost-effective finishing process for flat, cylindrical or profile-shaped hard surfaces. The addition of sanding material is from 0.1 to 0.2 mm and the surface roughness class from N3 to N6 can be achieved [3].

2 MATERIALS AND METHODS USED IN THE PROCESS OF ROBOTIC SANDING

2.1 Sander Mirka AIROS 650CV

A Mirka AIROS is an automatic, integrated, random orbital sander for industrial robots, in any industry with a need to automate surface finishing tasks. It is designed for intensive sanding with heavy loads, where precision and minimal maintenance are critical. Mirka AIROS is an electric and smart sander, built in a strong, but light aluminum housing, with a flange compatible with ISO 9409-1 for mechanical connection of robots. It can be adapted to all mechanical couplings, offering maximum flexibility.

The long-lasting brushless motor is particularly safe for wet sanding, and operates at a constant and adjustable rpm. This model has a 150 mm pad and needs to be connected to a dust extraction system.

The Mirka AIROS is the first main sanding attachment designed for use in automated robotic production for fine sanding. The main motion is eccentric rotation. It can be installed on most industrial manipulators on the market, and is light and compact. The model that was used in this paper is the Mirka airos 650CV, with a disc diameter of 150 mm, an eccentric of 5 mm and a speed of 4000-10000 rpm. Figure 3 shows the sander. [4]

Figure 3: *Mirka AIROS 650DV Sander [4]*

2.2 ABB IRB 4600 robot

The industrial manipulator to which the sander was connected is an ABB IRB 4600, shown in Figure 4. The IRB 4600 is a high productivity general purpose robot optimized for short cycle times, where compact robots can help create high productivity jobs. The IRB 4600 enables more compact production cells with increased production and higher quality – and this means improved productivity [5].

The IRB 4600 is the fastest palletizing robot in the world, capable of reducing cycle times significantly and increasing productivity. With a reach of 2.4 meters and a payload of 110 kg, this compact four-axis robot can achieve up to 2,190 cycles per hour with a load of 60 kg, which is 15 percent faster than its nearest competitor.

A small base area, acthin base radius around axis 1, the high mobility of axis 3, small lower and upper arms and compact wrist contribute to the most compact robot in its class. With the IRB 4600, a production cell with reduced floor space can be created by placing robots closer to the machines being served, which also increases output and productivity [5].

Figure 4: *ABB IRB 4600 robot [5]*

2.3 Force compensator FCU

Two representative force control methods have been proposed. They are impedance control [6] and hybrid position/force control [7]. The ABB robot and the Mirka sander are connected by a force compensator. It is possible to find only pneumatic force compensators on the market, which are, therefore, extremely expensive, both in terms of purchase and regular maintenance. Therefore, for the purpose of this research, in cooperation with the Faculty of Mechanical Engineering and Naval Architecure from Zagreb, we installed a custom made force compensator with an electric servomotor.

The force compensator is extremely important, because each manufactured tub deviates from the ideal model by a few millimeters. The reasons for this can be varied. From the type of acrylic, roving, the connection between the tub and the lining, to the weather conditions and the reaction of the tub during cooling and drying. The FCU device allows deviations from the ideal 3D model +/- 25mm. This is extremely important in production, because, in this way, we can detect a bad bathtub and a deviation from the ideal model. Also, in the case of human error and the

wrong selection of the sanding program, with the help of the sensor in the FCU, the robot stops, and no parts of the robot, sander or bathtub are broken.

Although it is so difficult and hard for skilled workers to keep the polishing force, tool position and orientation in the desired situation simultaneously, even for a few minutes, the robot sander can perform the task more uniformly and continuously. [8]

Figure 5: *Force compensator FCU*

3 RESULTS OF A ROBOTIC SANDING IMPLEMENTATION

From Table 1/Figure 4, we can see clearly that, with the introduction of robotic sanding, the consumption of sanding paper has almost halved. That may not seem like much when it comes to a freestanding bathtub, but the factory produces 1,000 freestanding bathtubs per week. That's about 50,000 tubs per year. Let's take into account the average price of sandpaper of 0,33 euros/piece + VAT. The annual consumption before the introduction of robotic sanding was about 500,000 pieces of sandpaper of all grain sizes, which is about 166,000 € + VAT. After the introduction of robotic sanding, the consumption of sanding paper decreased to about 350,000 pieces, which is about 116,000 € + VAT. This is a reduction of 30% per year. The savings on sandpaper were around 50,000 € + VAT. Paper consumption also varied greatly from worker to worker in manual sanding. The consumption of sandpaper was not the same between a worker who worked for several years and a worker who worked for a few days. Equally, it is easier for a worker to learn to manipulate a robot than to learn to sand, because the sanding of acrylic is very specific. The sanding robots have a barcode scanner that scans each tub. With this technique, the operator scans the barcode, the robot connects the barcode with the sanding program automatically and loads the program. Each tub has a sticker on the back that contains a bar code and the name of the tub. It is up to the operator to start the sanding cycle.

***Table 1**: Comparison of sandpaper consumption per bathtub*

No.	Bathtub type	Manual sanding	Robotic sanding
1	Wall 1a37 SLOT	5 pcs	3 pcs
2	Wall Corner L 1a37 SLOT	5 pcs	3 pcs
3	Form 1a37 SLOT	12 pcs	8 pcs
4	Cool 1a37 SLOT	10 pcs	8 pcs
5	Ideal Standard 180 1a28 SLOT	8 pcs	6 pcs

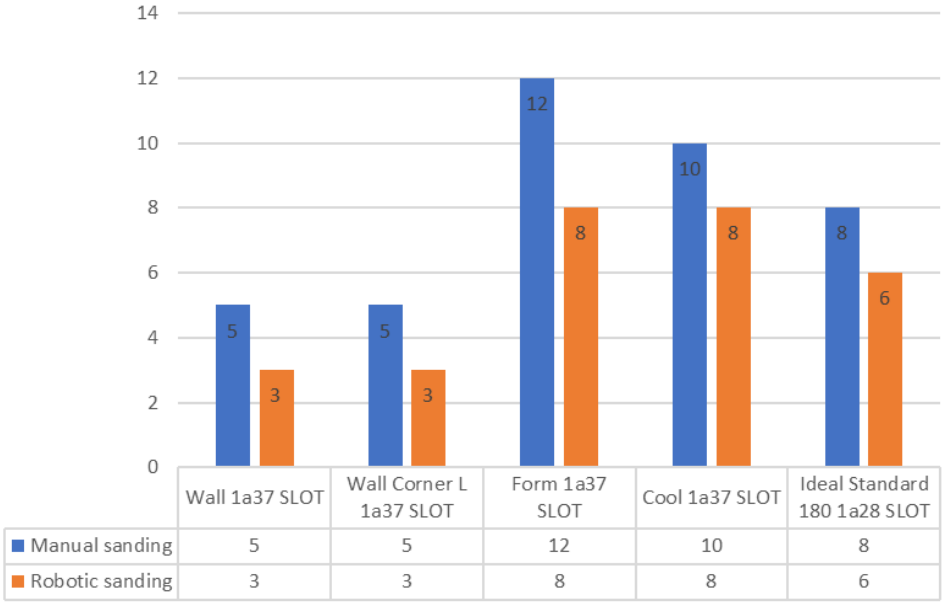

***Figure 4:** Comparison of sandpaper consumption*

Table 2/Figure 5 show the comparison of sanding times between manual and robotic sanding. Wall and Wall Corner bathtubs are the most common bathtubs produced by the Aquaestil factory. The average time for manual bathtub sanding is, depending on the sander, from 12 to 20 minutes, and robotic bathtub sanding takes 7 minutes, which is standardized. The time of robotic sanding is twice as short as the time of manual sanding. In May 2021, the factory increased the production of free-standing bathtubs from 550 bathtubs per week to 1,000 bathtubs per week, based on the purchase of 6 bathtub sanding robots. Of course, several people are also employed in other positions, where, due to the complicated production process, it is impossible to introduce robotization. In addition to speeding up the process and reducing the consumption of sandpaper with robotic sanding, it made it possible to facilitate the procurement of sandpaper, which is now standard, and the exact required amount of sandpaper can be known in advance. On average, one robot sands twice as many tubs as one worker. One operator drives two robots simultaneously. This means that labor saving by robotic sanding is four times greater than by manual sanding.

Table 2: *Comparison of sanding times*

No.	Bathtub type	Manual sanding	Robotic sanding
1	Wall 1a37 SLOT	15 min	7 min
2	Wall Corner L 1a37 SLOT	15 min	7 min
3	Form 1a37 SLOT	75 min	38 min
4	Cool 1a37 SLOT	60 min	33 min
5	Ideal Standard 180 1a28 SLOT	45 min	25 min

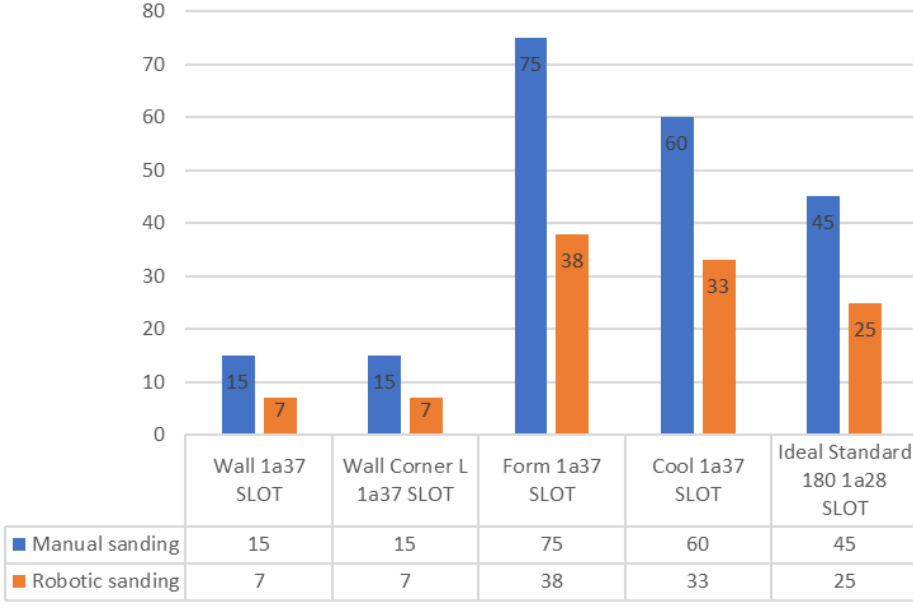

Figure 5: *Comparison of sanding times for different bath types*

4 CONCLUSION

Modern flexible production systems are designed for adaptive production with frequent and rapid changes, additions and improvements. By introducing robots into the production system, the time of product flow through the production process is reduced; product manufacturing time is shortened, i.e. productivity increases; it frees people from monotonous, difficult and dirty work and reduces the required working space. The human factor, which plays a major role in the number of downtimes, errors and, unfortunately, accidents in the production process itself, is being eliminated from production processes slowly by the use of robots. Robots can work 24 hours a day, 365 days a year with the same end result and minimal maintenance costs. With the introduction of robotic sanding in the manufacturing process of bathtubs, the production doubled, and the consumption of sandpaper almost halved, while accomplishing the same quality standards.

References

[1] **A. Gasparetto, L. Scalera:** *A Brief History of Industrial Robotics in the 20th Century*, Advances in Historical Studies, Vol.8 Iss.1, 2019. doi: 10[3.4236/ahs.2019.81002

[2] http://worldkings.org/news/world-creatorsfederation/top-100-global-creator-p81-george-devol-creator-of-first-industrial-robot. (28.09.2023)

[3] **L. Laperrière, G. Reinhart:** *CIRP Encyclopedia of Production Engineering*, Springer Berlin, Heidelberg, 2014

[4] https://www.mirka.com/en/p/Mirka-AIROS-650CV-150---5. (28.09.2023)

[5] https://new.abb.com/products/robotics/industrial-robots/irb-4600 (28.09.2023)

[6] **N. Hogan:** *Impedance control: an approach to manipulation: Part I–Part III. Trans ASME*, J Dyn Syst Meas Control 1985;107:1–24

[7] **M.H. Raibert, J.J. Craig.:** *Hybrid position/force control of manipulators*. Trans ASME, J Dyn Syst Meas Control 1981;102:126–33

[8] **F. Nagataa, Y. Kusumotob, Y. Fujimotob, K. Watanabec:** *Robotic sanding system for new designed furniture with free-formed surface*, Robotics and Computer-Integrated Manufacturin,g Vol. 23 p.p. 371–379, 2007. doi: doi.org/10.1016/j.rcim.2006.04.004

Journal of Energy Technology

Author instructions

http://www.fe.um.si/si/jet.htm

MAIN TITLE OF THE PAPER

SLOVENIAN TITLE

Author[1], Author [2], Corresponding author [ℜ]

Keywords: (Up to 10 keywords)

Abstract

Abstract should be up to 500 words long, with no pictures, photos, equations, tables, only text.

Povzetek

(Abstract in Slovenian language)

Submission of Manuscripts: All manuscripts must be submitted in English by e-mail to the editorial office at jet@um.si to ensure fast processing. Instructions for authors are also available online at http://www.fe.um.si/en/jet/author-instructions.html.

Preparation of manuscripts: Manuscripts must be typed in English in prescribed journal form (MS Word editor). A MS Word template is available at the Journal Home page.

A title page consists of the main title in the English and Slovenian language; the author(s) name(s) as well as the address, affiliation, E-mail address, telephone and fax numbers of author(s). Corresponding author must be indicated.

Main title: should be centred and written with capital letters (ARIAL bold 18 pt), in first paragraph in English language, in second paragraph in Slovenian language.

Key words: A list of 3 up to 6 key words is essential for indexing purposes. (CALIBRI 10pt)

[ℜ] Corresponding author: Title, Name and Surname, Organisation, Department, Address, Tel.: +XXX x xxx xxx, E-mail address: x.x@xxx.xx

[1] Organisation, Department, Address

[2] Organisation, Department, Address

Abstract: Abstract should be up to 500 words long, with no pictures, photos, equations, tables, - text only.

Povzetek: - Abstract in Slovenian language.

Main text should be structured logically in chapters, sections and sub-sections. Type of letters is Calibri, 10pt, full justified.

Units and abbreviations: Required are SI units. Abbreviations must be given in text when first mentioned.

Proofreading: The proof will be send by e-mail to the corresponding author in MS Word's Track changes function. Corresponding author is required to make their proof corrections with accepting or rejecting the tracked changes in document and answer all open comments of proof reader. The corresponding author is responsible to introduce corrections of data in the paper. The Editors are not responsible for damage or loss of submitted text. Contributors are advised to keep copies of their texts, illustrations and all other materials.

The statements, opinions and data contained in this publication are solely those of the individual authors and not of the publisher and the Editors. Neither the publisher nor the Editors can accept any legal responsibility for errors that could appear during the process.

Chapter examples:

1 MAIN CHAPTER (Arial bold, 12pt, after paragraph 6pt space)

1.1 Section (Arial bold, 11pt, after paragraph 6pt space)

1.1.1 Sub-section (Arial bold, 10pt, after paragraph 6pt space)

Example of Equation (lined 2 cm from left margin, equation number in normal brackets (section.equation number), lined right margin, paragraph space 6pt before in after line):

Equation (1.1)

Tables should have a legend that includes the title of the table at the top of the table. Each table should be cited in the text.

Table legend example:

Table 1: *Name of the table (centred, on top of the table)*

Figures and images should be labelled sequentially numbered (Arabic numbers) and cited in the text – Fig.1 or Figure 1. The legend should be below the image, picture, photo or drawing.

Figure legend example:

Figure 1: *Name of the figure (centred, on bottom of figure, photo, or drawing)*

References

[1] **N. Surname:** *Title,* Journal Title, Vol., Iss., p.p., Year of Publication

[2] **N. Surname:** *Title,* Publisher, Year of Publication

[3] **N. Surname:** *Title* [online], Publisher or Journal Title, Vol., Iss., p.p., Year of Publication. Available: website (date accessed)

Examples:

[1] **J. Usenik**: *Mathematical model of the power supply system control*, Journal of Energy Technology, Vol. 2, Iss. 3, p.p. 29 – 46, 2009

[2] **J. J. DiStefano, A.R. Stubberud, I. J. Williams**: *Theory and Problems of Feedback and Control Systems*, McGraw-Hill Book Company, 1987

[3] **T. Žagar, L. Kegel**: *Preparation of National programme for SF and RW management taking into account the possible future evolution of ERDO* [online], Journal of Energy Technology, Vol. 9, Iss. 1, p.p. 39 – 50, 2016. Available: http://www.fe.um.si/images/jet/Volume 9_Issue1/03-JET_marec_2016-PREPARATION_OF_NATIONAL.pdf (7. 10. 2016)

Example of reference-1 citation: In text *[1],* text continue.

Nomenclature

(Symbols)	(Symbol meaning)
t	time

JET

JET I Journal of Energy Technology I Vol. 16, Issue 3, November 2023 I University of Maribor, Faculty of Energy Technology

ISSN 1855-5748

9 771855 574008